# UNIVERSIDAD DE SONORA

DIVISIÓN DE CIENCIAS EXACTAS Y NATURALES

**Programa de Maestría en Ciencias (Física)**

## "Characterization of Hydrodynamic Simulations Generated by Particle Splitting"

## Thesis

Submitted to the graduate degree program in Physics in partial fulfillment of the requirement for the **Degree of Master of Science**

By:

José Carlos González Martínez

Director:

Guillermo Arreaga García

Hermosillo, Sonora

October 2020

# Universidad de Sonora

Repositorio Institucional UNISON

"El saber de mis hijos
hará mi grandeza"

# Products

The present thesis is one of the products obtained from two years of research as well as the article titled "A Particle Splitting Method to Generate New Turbulent Simulations of collapsing gas cores" which has been submitted elsewhere

# Acknowledgements

# Abstract

The study of gravitational collapse of dense gas clouds is performed using the basic theory of self-gravitational hydrodynamics to follow the evolution of a self-gravitating, inviscid, compressible, non-magnetic fluid. The numerical method Smoothed Particle Hydrodynamics (SPH) is used to establish the equations of self-gravitational hydrodynamics for numerical treatment and the publicly available code Gadget2 to solve the equations. The physical systems consist in a gas cloud with rigid-body rotation and a gas cloud with induced turbulence. To follow the evolution of a gas cloud under gravitational collapse, it is necessary to have adequate resolution at all times to be able to obtain physically reliable results. To enhance the resolution on regions of high density, the Particle Splitting technique is used. The main idea of this technique is to achieve enhanced resolution by replacing each particle in the region of interest for a set of new finer particles. A comparative study is made to decide whether Particle Splitting is able to reproduce the output of the original simulations but with improved resolution or if it gives outputs with biased results. After a series of simulations with and without Particle Splitting upon both physical systems, the outputs give models with enhanced resolution showing more substructure within the cores compared to the simulations without Particle Splitting.

*Subject headings:* -stars: formation; -physical processes: gravitational collapse, hydrodynamics; -methods: numerical.

# Resumen

El estudio del fenómeno de colapso gravitacional en nubes densas de gas es realizado usando la teoría básica de la hidrodinámica autogravitante la cual nos permite seguir la evolución de un fluido autogravitante no viscoso, compresible y no-magnético. Usando el método numérico de Hidrodinámica de Partículas Suavizadas (SPH) se establecen las ecuaciones de la hidrodinámica autogravitante en su formulación numérica y el código público Gadget2 para la solución de las ecuaciones. Los sistemas físicos consisten en una nube de gas con rotación de cuerpo rígido y una nube de gas con turbulencia inducida. Al seguir la evolución de una nube de gas bajo severo colapso gravitacional, es necesario tener resolución adecuada para poder obtener modelos con resultados físicos confiables. Para aumentar la resolución en regiones de alta densidad, se usa la técnica de Particle Splitting. La idea principal de esta técnica es la de mejorar la resolución al sustituir cada partícula en la región de interés por un conjunto de nuevas y más finas partículas. Se hace un estudio comparativo para saber si Particle Splitting es capaz de reproducir los resultados de la simulación original, pero con resolución incrementada o si se obtienen resultados diferentes. Después de una serie de simulaciones con y sin Particle Splitting en los dos sistemas físicos, los resultados arrojan modelos con resolución aumentada al aplicar la técnica, mostrando más subestructura en los núcleos formados en comparación con las simulaciones sin Particle Splitting.

*Palabras clave:* -estrellas: formación; -procesos físicos: colapso gravitacional, hidrodinámica; -métodos: numérico.

# CONTENTS

# List of Figures

# List of Tables

# Introduction

Numerical simulations play a very important role in astrophysics nowadays. With this tool, theoretical and observational studies complement each other to study any physical phenomenon in the Cosmos. Star formation is one of the branches of astronomy that relies heavily on numerical simulations given the wide dynamic ranges in space, time and densities. Gravitational collapse is the central physical process in star formation, beginning on the largest scales when perturbations form dense seeds which might eventually be the first protostars. The physics of star formation, and specifically the process of gravitational collapse, is commonly studied with numerical methods. Smoothed Particle Hydrodynamics (SPH) is a Lagrangian numerical method used to discretize the hydrodynamical equations to be solved so that it can be treated on computers to follow the evolution of the systems. To simulate this process, the problem of the spatial resolution always arises which depends on the total number of particles used in the simulation. When following the evolution of the system, resolution is sometimes insufficient due to the increase of local density and some valuable information about the structures and formations within the system is lost.

The relevance of turbulence is notably since it plays a very important role in the theory of star formation. It is presumably responsible for the structures and dynamics of molecular clouds by shaping, morphing, and fragmenting them (Ballesteros-Paredes et al. 1999a). Much of this might be related to the velocity fields with high Reynolds numbers, where turbulence is evident. Some authors even have argued that turbulence plays a crucial role providing global support against collapse, while promoting local collapse where motions are converging (Vazquez-Semadeni 2018). In recent years, much work has been done on this subject which spans from the large length-scale of supersonic turbulence on the formation of molecular clouds (Vazquez-Semadeni 2006; Vazquez-Semadeni 2007; Vazquez-Semadeni 2010; Vazquez-Semadeni 2018) to the occurrence of fragmentation during the collapse of

these giant clouds, to form stellar clusters, (Klessen et al. 2000; Klessen et al. 2001) to smaller-length scales where subsonic turbulence favor the collapse and fragmentation of low-mass cores to form binary systems (Goodwin et al. 2004a; Goodwin et al. 2004b; Goodwin et al. 2006).

Kitsionas and Whitworth (2002) in the search for a way of following the evolution under a severe gravitational collapse with adequate resolution on high-density regions, they developed the Particle Splitting technique, which is based on the idea of increasing the resolution on regions of interest. This is done by increasing locally the number of particles so that the resolution is adequate and gives reliable results. The way to increase the number of particles is by replacing a single particle of the original simulation by a set of finer particles located in a specific configuration. Such configuration is called a unit cell. Kitsionas & Whitworth (2002) used a unit cell containing 12 particles on a hexagonal configuration.

It is worth mentioning that particle splitting together with particle merging was originally invented to preserve the resolution on regions of low-density (Meglicki, Wickramasinghe & Bicknell 1993) or to avoid the use of large number of particles on high-density regions (Bate et al. 1995), however, Kitsionas & Whitworth made a novel use of particle splitting and this is the approach followed in this thesis. Some up-to-date work can be consulted on the literature about simulations of star formation using particle splitting, for example (Ray-Raposo 2015) and (Bending et al. 2020).

In the present work, a series of simulations of the formation of dense gas cores by gravitational collapse using particle splitting is performed with two main objectives: 1) to study the structures formed and identify some of their features that also are reported in observations and theoretical literature as well as in other simulations performed in the past (Boss & Bodenheimer 1979; Kitsionas & Whitworth 2002; Boss et al. 2000) and 2) perform simulations with improved resolution on regions where all the features of the structures formed can be visualized and analyzed saving computational time in the generation of the initial conditions. The approach used here is similar to that of Kitsionas & Whitworth (2002),

but rather than using a hexagonal unit cell, a unit cell based on the zinc sulfide (SZn) molecule is used instead.

Particle splitting is applied on two variants, one applying the technique upon all the particles of the simulation so, for example, if an original simulation is built-up of 996,972 particles, after applying particle splitting, the total number of particles will increase to 17,945,496. The second variant is applying particle splitting upon a subset of particles the ones that reach a threshold density value so that resolution is enhanced on those specific regions where substructure forms within the core.

The physical systems studied in this work are, on one side, a dense gas core with rigid-body rotation with an initial periodic mass perturbation which triggers the collapse, and on the other, a gas core with turbulence generated as a superposition of Fourier modes. The former has been studied in the past by many authors; Burkert & Bodenheimer (1993), Bate & Burkert (1997), Boss et al. (2000), Truelove et al. (1998), Klein et al. (1999), Kitsionas & Whitworth (2002) and Springel (2005) but the one that has gained the recognition as the standard simulation for isothermal collapse is the one developed by Boss & Bodenheimer (1979). This also has been reproduced in this work with standard resolution for the sake of comparison with the models here developed, so one can decide whether the results obtained are reliable or not.

With respect to the turbulent models, the computational cost in the generation of the initial conditions of the turbulent spectrum is very high such that it takes 50 hours for a simulation of 1,000,000 particles on a serial code (Arreaga-Garcia 2017). For a parallel code, a simulation of 10,000,000 particles running in 80 processors will need 8 hours (Arreaga-Garcia 2017). The correct implementation of particle splitting technique can change this.

All models are set with the dimensionless ratios $\alpha$ and $\beta$, defined as the ratio of thermal energy to gravitational potential energy and the ratio of the kinetic energy to gravitational potential energy respectively, so that they represent the physical state of the gas structures on the verge of collapse.

This work is organized as follows: In Chapter 1 is presented the observational and theoretical background upon which the study of gravitational collapse in star formation is based. A brief review about observed objects on regions of star formation is given so as the rotational and turbulent conditions in molecular clouds. Then, the energy stability analysis for the requirement of gravitational collapse is described, and finally the Jeans condition and the mass resolution requirement.

In Chapter 2, the basic equations that are involved in the study of the evolution of a self-gravitating fluid are introduced. The numerical method Smoothed Particle Hydrodynamics (SPH) and the Gadget2 code that is used to solve the equations for gravitational collapse are presented and then, some details of the integration schemes applied by Gadget2 are provided. Finally, the particle splitting technique is introduced just as the unit cell.

The physical systems are introduced in Chapter 3 and a description of how the particle splitting technique is applied is given. The generation of a trial model is carried out to help the visualization of the implementation of the unit cell. Then, the physical system is introduced together with the physical parameters. The models and the implementation of the unit cell on the models are lastly explained.

In Chapter 4 the results of the simulations for both the rotational and turbulent systems are discussed and compared with those with no particle splitting. First, for the models at initial time $t = 0$. Density distribution plots generated with PV-WAVE are shown, where one can see the visual initial configurations of the systems. Then, for the final evolution time $t = t_{final}$ where one can see the substructures formed after the process of collapse. With the aid of $log(\rho_{max})$ versus $t$ plots for the various models, comparison between them with and without particle splitting are made. At the end of this section, the turbulent behavior of the models is discussed and compared with those without particle splitting.

Chapter 5, Discussion and Conclusions summarize the results whether the particle splitting technique was able to reproduce, in general, the results of the original models or if there was a bias from them. At the end, some thoughts about the evolution of the turbulence in turbulent cores are made and comparison with results in the literature.

# Chapter 1 – Observational and Theoretical Background

Measurements of specific physical quantities give information about the conditions present in every stage of the whole process of star formation and help to corroborate theoretical and numerical models. Of main importance for the present work are the initial conditions of the environment and physical processes that trigger gravitational collapse that will be set on the numerical models so that they form, at the end to the evolution time, condensed protostellar objects. Observational measurements of length scales, density distributions and velocities of some objects on these regions give some of this valuable information. Also, of great importance is the data output of the simulations that fit the observations.

This first section provides some of the observational evidence related to star formation in molecular clouds and a brief summary about observed physical parameters such as length scales, masses, temperatures, number density of particles as well as measurements of velocities by doppler-broadening of molecular lines. At the end, a review about the physical state of the clouds including rotation and turbulence for instance, typical values of angular velocities of cloud cores, examples of observations of rotation in molecular clouds, subsonic and supersonic turbulence at various scales, the Larson relation of velocity dispersion to length scale, important points about structures developed, and mechanisms of dissipation of turbulence.

## 1.1 Observational evidence of star formation on molecular clouds

Star formation has been observed to occur in molecular clouds, which are regions of cold and dense gas and dust. Molecular clouds are subdivided arbitrarily into clumps that are observed in CO molecular line. These clumps may have masses in the range $10^3 - 10^4\ M_\odot$, radii of 2 – 5 parsec, temperature of 10 K, mean number density of $H_2$ of $10^2 - 10^3 cm^{-3}$, magnetic

field of $3 \times 10^{-5}$ gauss (Bodenheimer 2011). The velocities are determined by measuring the molecular line widths with Doppler-broadening. For thermal motion, this velocity is about 0.2 km/s, however, due to large-scale motions, probably turbulent and/or magnetic effects, velocities are in the range of $2 - 3$ km/s (Bodenheimer 2011).

Within the clumps, high-density cores can be observed in the $NH_3$, CS and other molecular lines. These objects may have masses about ~1 to few solar masses, some to $1,000 M_\odot$, sizes ~$0.05 - 0.1$ pc, temperature of 10 K, density ~$10^4 - 10^5\ cm^{-3}$ (Bodenheimer 2011).

One region of interest for the study of star formation is Taurus-Auriga, illustrated in figs 1.1 and 1.2. There can be found a rich population of young pre-main sequence stars known as T Tauri. Most T Tauri stars are bright optical variable with G, K and M spectral types (Kenyon, Gomez, Whitney 2008). Other objects found in Taurus-Auriga are ammonia cores, infrared sources observed by IRAS (Infrared Astronomical Satellite) and bipolar CO outflows. There are starless regions where infall motions have developed suggesting that these may eventually form low-mass stars given the positional correlation with respect the other objects (Bodenheimer 2011).
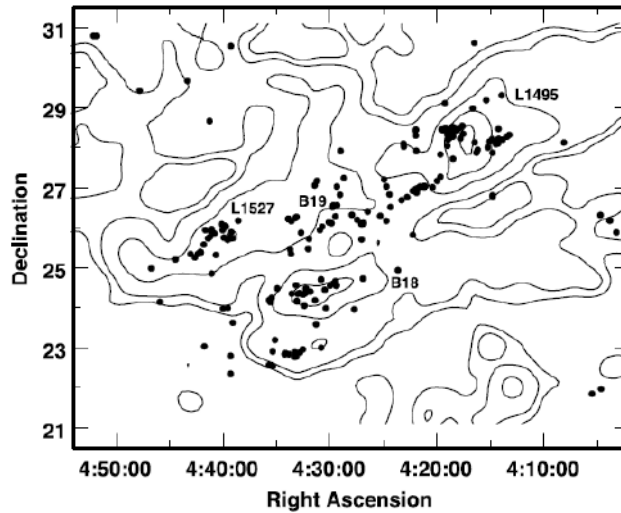


Fig. 1. 1 "Sky map for the center of the Taurus-Auriga region in J2000 coordinates. Solid contours indicate CO column densities from Ungerechts & Thaddeus (1987); the levels are 3, 5, 10, 15, and 20 K km/s. Solid points indicate the positions of pre-main sequence stars. Groups of young stars lie in L1495 (NW; RA = 4h 12m.4h 20m, Dec = 27° - 29°), B18/L1529 (center; RA = 4h 24m. 4h 36, Dec = 23° - 25°), B19/L1521 (center; RA = 4h 24m.4h 36, Dec = 25°-27°), and L1527-29, L1534-35 (E; RA = 4h 36m.4h 44, Dec = 24°- 26°). Only a few young stars lie outside the densest molecular gas". Image retrieved from Kenyon, Gomez, Whitney (2008).
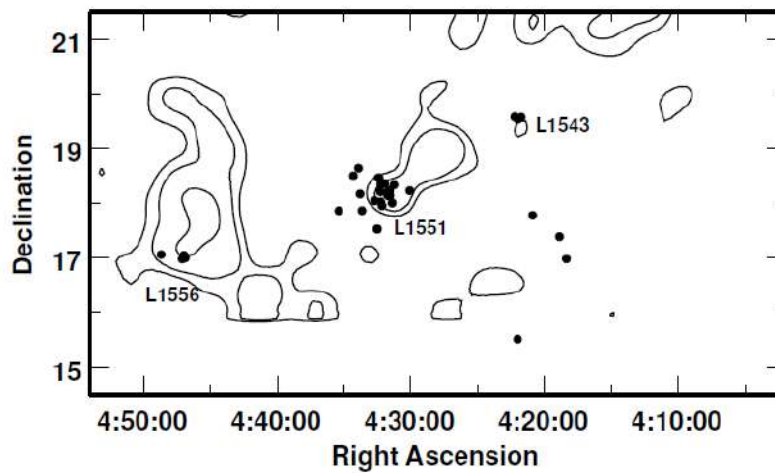
Fig. 1. 2 "Southern portion of the Taurus-Auriga region. Groups of young stars are heavily concentrated in the L1551 dark cloud (RA = 4h 31m, Dec = 18°), with a few stars in L1543 (RA = 4h 23m, Dec = 19°) and L1556 (RA = 4h 46m, Dec = 17°)". Image retrieved from Kenyon, Gomez, Whitney (2008).

The object L1551, which is shown in fig. 1.2, is formed by L1551 IRS5, the protostar L1551 NE, and a few deeply embedded T Tauri stars (Kenyon, Gomez, Whitney 2008). L1551 includes features like a disk observed in CS molecular line, an embedded infrared source, a reflection nebula which reveals some of the underlying star and optical emission regions which correspond to collimated jets near the star and also to Herbig-Haro (HH) objects (Bodenheimer 2011).

Some individual objects of interest in the Taurus-Auriga region are the star T Tauri. This is the prototype of young, low-mass variable stars and it is located in the most southern of Taurus-Auriga dark clouds (Kenyon, Gomez, Whitney 2008). There are two components, T Tau N and T Tau S which are shown in fig. 3. T Tau N is the saturated point source surrounded by a dark halo. T Tau S is the fuzzy source due to south and is a binary whose components are T Tau Sa an Sb. It's estimated distance is of 147.6±0.6 pc (Kenyon, Gomez, Whitney 2008).

L1551 IRS5, shown in fig. 1.4, is a very red young star, source of a bipolar outflow (Kenyon, Gomez, Whitney 2008). The flow consists of a short jet and numerous faint knots and bow

3

shocks. Both binary components appear to drive outflows, which interact and merge to form the majestic large-scale outflow structure. Some knots and bow shocks are associated with the nearby young stars L1551 NE and HH30 IRS (Kenyon, Gomez, Whitney 2008).
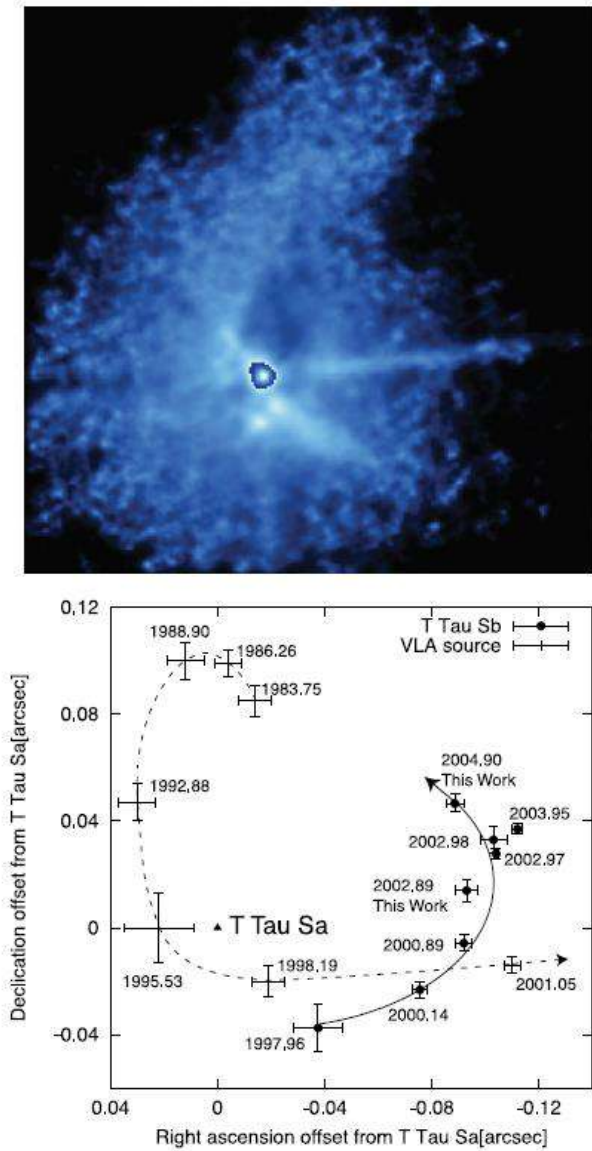


Fig. 1. 3 "The T Tauri binary. *Upper panel:* 1000x 1000 optical image (C. & F. Roddier). T Tau N is the saturated point source surrounded by a dark halo. T Tau S is the fuzzy source due south. At PA = 315° from T Tau, the slightly elongated blob is a bright radio source (Ray et al. 1997). Two collimated jets appear to emanate from T Tau N, one with PA $\approx$ 45° and 225° and another with PA $\approx$ 270°. The bright spike at PA $\approx$ 270° points to Hind's nebula, ~45'' to the west. *Lower panel:* Motion of the T Tau S binary from Mayama et al. (2006). T Tau Sa and T Tau Sb appear to form a bound pair; the VLA source is probably not bound to this pair (see also Kohler et al. 2008)". Image retrieved from Kenyon, Gomez, Whitney (2008).
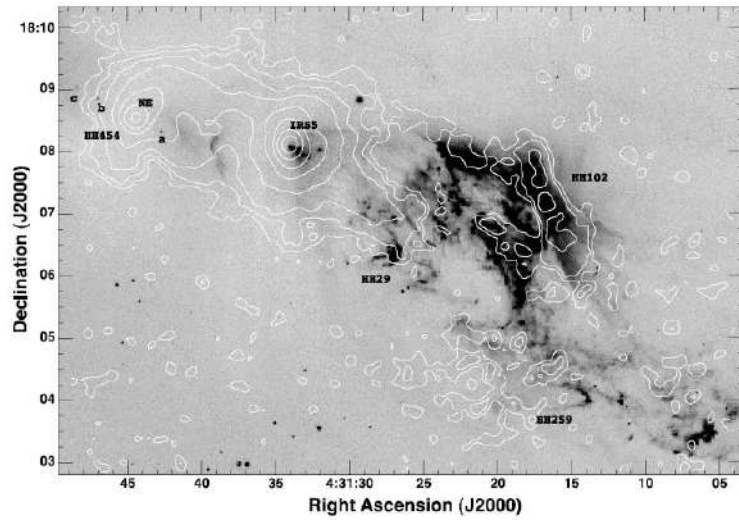
Fig. 1. 4 "[S II] image of L1551 IRS5 with contours of 850 _m emission overlaid (Moriarty-Schieven et al. 2006). The contour levels are 0.02, 0.04, 0.08, 0.16, 0.32, 0.64, 1.28, and 2.56 Jy beam$^{-1}$". Image retrieved from (Kenyon, Gomez, Whitney 2008).

Other more isolated regions that are likely sites of star formation are the Bok globules. The globule Barnard 68, taken by Bart Bok, is illustrated in fig. 1.5. Its radius is about 0.05 pc. Observations indicate that the distribution of masses of the cores is very similar to that of the initial mass function of stars (Bodenheimer 2011).
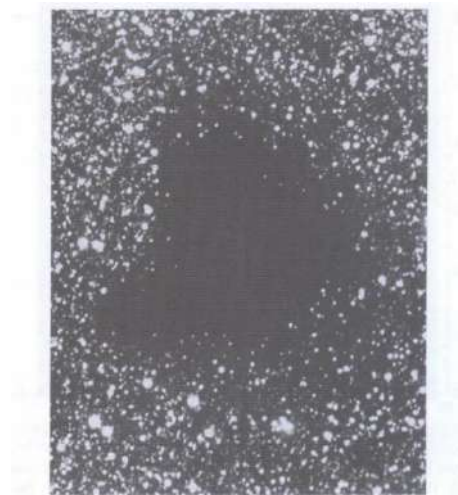


Fig. 1. 5. "Optical photograph of the Bok Globule Barnard 68. The almost total lack of stars near the center of the globule suggests a visual extinction of more than 25 magnitudes". Adapted from "Principles of Star Formation" (p 15) by P. Bodenheimer. Springer-Verlag Berlin Heidelberg, 2011.

## 1.2 The physical conditions of the clouds

### *1.2.1 Rotation*

Rotation is measured in molecular clouds and cloud cores through the observation of a gradient in the radial velocity $dv/ds$ where s is the distance in the plane of the sky. This gradient is measured at various points across the cloud. Uniform rotation is present when there is a linear velocity variation with spatial coordinate across the cloud. Thus, the approximations $\Omega \approx dv/ds$ and $j \approx 0.4\Omega R^2$ from the velocity gradient and from models of uniform rotation consistent with observations within errors, can be made (Bodenheimer 2011). However, the inclination angle of the rotation axis to the line of sight is unknown. On the cloud core scale, the typical values of $\Omega$ are $10^{-13} - 10^{-14}\ s^{-1}$. One example of rotation detected at protostellar scales, in CS measurements, is that on the protostellar binary IRAS 16293-2422, fig. 1.3, which has two components separated by about 800 AU. The lines of the molecule CS show a gradient in the line-of-sight component of the velocity, along the axis connecting the two components. The conclusion is that a rotating circumbinary disk is present, with a radius of several thousand AU.

Rotation does not appear to be a major factor in the support of cloud against collapse. In spite of this, there is an angular momentum problem as was stated by Spitzer: Consider a gas cylinder 10 pc long with 0.02 pc of radius, density of $5 \times 10^{-23}\ gcm^{-3}$, mass of one solar mass, rotating about its long axis at $10^{-15}s^{-1}$. Contraction is parallel to $J$ no opposed by rotation. To reach stellar size, the radius must contract 7 orders o magnitude. If angular momentum is conserved, $\Omega R^2 = $ constant, $\Omega$ increases 14 orders of magnitude to $10^{-1}s^{-1}$. Then the rotational velocity would be $6 \times 10^9 cms^{-1}$ or 0.2c. The centripetal acceleration would be $10^4$ times that of gravity.
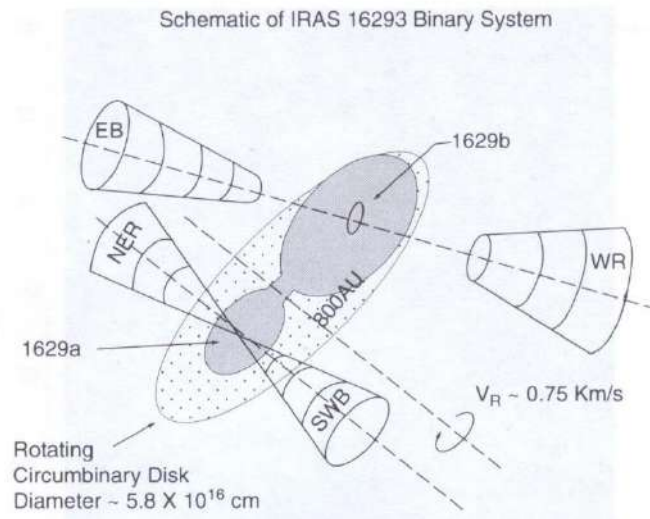
Fig. 1. 6. "Schematic diagram of a binary protostar. The two components 1629a and 1629b are in orbit, with the orbital angular momentum along the dashed line passing between the two objects. Each of the components has a small disk around it, and the angular momenta of the disks are not parallel. The component 1629a is driving a bipolar outflow, indicated by the cones NER and SWB. The component 1629b was driving an outflow in the past but is not currently doing so. Both sources are embedded in a circumbinary disk which may not be in equilibrium, rather, still falling. Darker/lighter shading indicates higher/lower dust column density between observer and source". Adapted from "Principles of Star Formation" (p 15) by P. Bodenheimer. Springer-Verlag Berlin Heidelberg, 2011.

### 1.2.2 Turbulence

The study of turbulence of both molecular cloud and protostellar scales involves subsonic and supersonic motions and the whole spectrum in between. The Reynolds number $R_e = vL/v$ provides a general criterion for the onset of turbulence, which is normally about several thousand. In general terms, energy is fed into the turbulence on the largest scales and it cascades to smaller until it dissipates into heat. The typical velocity to length scale relation that concerns turbulence is the Kolmogorov law which is of the form $v \propto L^{1/3}$. From Larson's findings this relation is $v \propto L^{1/2}$ (Bodenheimer 2011). Thus, most of the kinetic energy lies on the largest scales.

The possible origins of turbulence on molecular clouds are 1) Instabilities induced by colliding flows in the interstellar gas 2) Magnetorotational instabilities in galactic disks 3) Instabilities that develop behind the spiral waves in the galaxy (Bodenheimer 2011). What is

for sure is that the energy input is not limited to the largest scales, also the dissipation mechanisms are not limited to the smallest scales. The key to star formation by turbulent effects are the transient compression of certain regions by shockwaves. They can become Jeans unstable and begin to collapse.

It is worth mentioning that the origin and effects of turbulence in the formation of condensed cores is a very active area of research nowadays and can be found in (Xu & Lazarian 2020; Vazquez-Semadeni 2020; Robertson & Goldreich 2012; Price & Federrath 2010) among others.

## 1.3 Stability Analysis for Gravitational Collapse

The first derivation of the physical requirement that a region of a molecular cloud must fulfill before it can collapse was done by Sir James Jeans. His analysis was based on linear stability performed on the basic equations of hydrodynamics. Another approach can be taken by requiring that the gravitational potential energy must exceed the sum of the thermal, rotational, turbulent and magnetic energies (Bodenheimer 2011)

$$\left|E_{grav}\right| > E_{th} + E_{rot} + E_{turb} + E_{mag} \tag{1.1}$$

This analysis is for a mass $M$ of gas that is gravitational bounded. For this mass to be of order of $M_{\odot}$, the collapse must be triggered on the coolest and densest parts of the interstellar medium.

For an assumed spherical configuration,

$$E_{grav} = -C_{grav}\frac{GM^2}{R} \tag{1.2}$$

where $C_{grav}$ is a constant depending on the mass distribution and equals 3/5 for uniform density. The total thermal energy for an isothermal ideal gas with temperature is

$$E_{th} = \frac{3}{2}\frac{R_g TM}{\mu} \tag{1.3}$$

where $R_g = k_B/m_u$ is the gas constant, $k_B$ is the Boltzmann constant, $m_u$ is the atomic mass unit, and $\mu$ is the molecular weight of the gas in atomic mass units. The rotational energy is

$$E_{rot} = C_{rot}MR^2\Omega^2 \tag{1.4}$$

for an assumed uniform angular velocity $\Omega$, where $C_{rot}$ depends on the mass distribution and equals 1/5 for uniform density. The turbulent kinetic energy is

$$E_{turb} = \frac{1}{2}M\sigma^2 \tag{1.5}$$

where $\sigma$ is the mean turbulent velocity. The magnetic energy is given by the volume integral

$$E_{mag} = \frac{1}{8\pi}\int B^2 dV \approx \frac{1}{6}B^2R^3 \tag{1.6}$$

where $B$ is the assumed uniform magnetic field.

Considering a uniform-density, uniform-temperature sphere to be gravitationally bound $\left[(3/5)GM^2/R = (3/2)R_gTM/\mu\right]$ the Jeans length reads:

$$R_J = \frac{0.4GM\mu}{R_gT} \tag{1.7}$$

where $\mu \approx 2.37$ for solar composition with molecular hydrogen. For a cloud of a given mass and temperature, the radius must be smaller than $R_J$ to be unstable to gravitational collapse. To obtain the Jeans mass, which is the minimum mass that the cloud of given $\rho$ and T must have to be unstable, the radius can be eliminated from (1.7) in favor of the density $\rho$, assuming again that the gas is a sphere

$$M_J = \left(\frac{5}{2}\frac{R_gT}{\mu G}\right)^{3/2}\left(\frac{4}{3}\pi\rho\right)^{-1/2} = 8.5 \times 10^{22}\left(\frac{T}{\mu}\right)^{3/2}\rho^{-1/2}g \tag{1.8}$$

Another commonly used version of the Jeans length is obtained by eliminating the mass in (5) in favor of density and radius:

$$R_J \approx \left(\frac{R_g T}{\mu}\right)^{1/2} \frac{1}{\sqrt{G\rho}} \approx c_s t_{ff} \tag{1.9}$$

where $c_s$ is the isothermal sound speed and $t_{ff}$ is the free-fall time. Here, given T and $\rho$, the radius of the cloud must be larger than $R_J$ for collapse to occur.

Now consider rotational effects in addition to thermal effects and gravity. The ratios $\alpha = E_{th}/|E_{grav}|$ and $\beta = E_{kin}/|E_{grav}|$, where the density of the sphere and its angular velocity $\Omega$ are assumed constant. The revised expression for the Jeans mass becomes

$$M_J = \left(\frac{\frac{3R_g T}{2\mu} + 0.2\Omega^2 R^2}{0.6G}\right)^{3/2} \left(\frac{4}{3}\pi\rho\right)^{-1/2} \tag{1.10}$$

and $M > M_J$ is the requirement for the cloud to collapse.

## 1.4 The Jeans Condition and Spatial Resolution

Truelove et al. (1997) propose the spatial resolution of the simulations as a criterion of validation of the calculations and it is directly related to the stability analysis performed by James Jeans. In fact, both concepts are intimately related, yet the former being intrinsic of the numerical method and the latter, a condition or requirement inherently of the physical process.

In their study, Truelove et al. (1997) demonstrated with a three-dimensional hydrodynamic simulation code with adaptive mesh refinement (AMR), that the perturbations originated by the discretization of the equations of hydrodynamics for the gravitational collapse may generate fragments, a process they called *artificial fragmentation*. If the Jeans length is larger than the cell, size perturbations grow unstable. The unstable growth is inherently of the physical process, nevertheless, the origin of the perturbation is purely numeric.

This effect, which pollutes the solution, can be reduced significantly and possibly eliminated ensuring that the relation of the size of the cell to the Jeans length is kept below 1/4.

This relation is called the Jeans Number

$$J \equiv \frac{\Delta x}{\lambda_J} \tag{1.11}$$

And the requirement

$$J < 1/4 \tag{1.12}$$

is called the *Jeans condition*.

## 1.5 Mass Resolution

Bate and Burkert (1997) demonstrated that there is a Jeans condition similar for particle-based simulations introducing the concept of resolvable mass $M_{min}$. Thus, the Jeans condition reads as

$$2M_{min} \leq M_J \tag{1.13}$$

where $M_{min} = \mathcal{N}_{neig}m$ with $\mathcal{N}_{neig}$ being the number of SPH neighboring particles as will be introduced in Chapter 2 and $M_J$ as defined in section 1.3.

For a region whose Jeans condition is not satisfied, artificial fragmentation will occur and the real fragmentation will be suppressed. An example of the isothermal collapse simulation with different resolutions from $3.3 \times 10^4$ particles to $1.71 \times 10^7$ in factors of 8 (Springel 2005) is shown in fig 1.7.
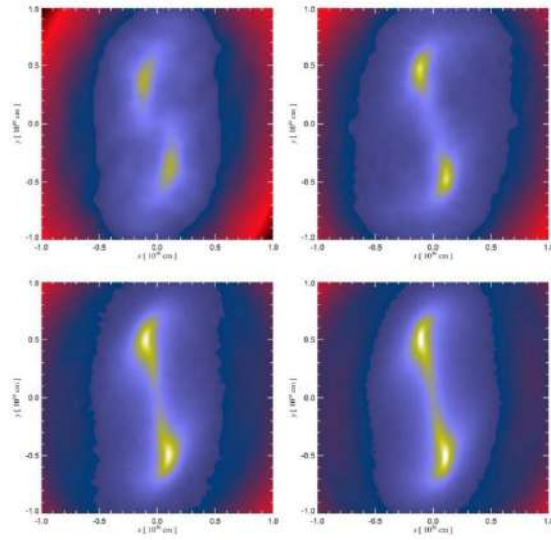
Fig. 1. 7. "Resolution study for the 'standard isothermal collapse simulation'. The gas density is shown in a slice through the centre of the simulated volume at 1.24 free fall times, roughly when the two perturbations at the ends of the bar-like structure become self-gravitating and undergo gravitational collapse. From the top left to the bottom row, the particle number increases from $3.3 \times 10^4$ to $1.71 \times 10^7$ by factors of 8". Adapted from Springel, V. (2005). The cosmological simulation code GADGET-2. *Monthly notices of the royal astronomical society*, *364*(4), 1105-1134.

# Chapter 2 – Computational Methods

In this chapter, the underlying analytical and numerical basis, upon which simulations of gravitational collapse are built up, are exposed beginning with a review of the system of equations needed to be solved in order to follow the evolution of a collapsing system. Then, the numerical method Smoothed Particle Hydrodynamics (SPH) is introduced with the basic definition of a SPH quantity using the summation interpolation technique (Monaghan 1992). Then, the set of equations involved in gravitational collapse are presented in SPH formulation. Finally, the evolution code Gadget2 is introduced by showing the set of equations solved by Gadget2, details about the gravitational algorithms applied to compute the gravitational forces and the time integration schemes.

## 2.1 Self-gravitational hydrodynamics

In order to describe the evolution of a self-gravitating, inviscid, compressible, non-magnetic fluid, we need to solve a system of four equations -the continuity equation, Euler's equation, the energy equation and an equation of state (Landau & Lifshitz 1966; Shu 1992) – with four unknows, namely the velocity $v$, pressure $P$, specific internal energy $u$, and density $\rho$, at each position $r$ in the fluid. The four equations read as follows:

- Continuity equation

$$\frac{d\rho(\boldsymbol{r})}{dt} = -\rho(r)\nabla \cdot \boldsymbol{v}(\boldsymbol{r}) \tag{2.1}$$

where the Lagrangian derivative with respect to the time $\frac{d}{dt} = \frac{\partial}{\partial t} + v \cdot \nabla$ and $\frac{\partial \rho}{\partial t} = -\nabla \cdot (\rho v)$ is used. The continuity equation expresses the conservation of mass.

- Euler's equation

$$\frac{d\boldsymbol{v}(\boldsymbol{r})}{dt} = -\frac{1}{\rho(\boldsymbol{r})}\nabla P(\boldsymbol{r}) + \boldsymbol{a}_{grav}(\boldsymbol{r}) + \boldsymbol{a}_{visc}(\boldsymbol{r}) \tag{2.2}$$

where $\boldsymbol{a}_{grav}$ is the self-gravitational acceleration and it's given by

$$\boldsymbol{a}_{grav}(\boldsymbol{r}) = G \int_{all\ space} \frac{\rho(\boldsymbol{r}')(\boldsymbol{r}' - \boldsymbol{r})d^3\boldsymbol{r}'}{|\boldsymbol{r}' - \boldsymbol{r}|^3} \tag{2.3}$$

Euler's equation expresses the conservation of momentum.

- Energy equation

$$\rho(r)\frac{du(\boldsymbol{r})}{dt} = -P(r)\nabla \cdot \boldsymbol{v}(\boldsymbol{r}) + (\Gamma - \Lambda) \tag{2.4}$$

Where $\Gamma$ and $\Lambda$ are the radiative heating and cooling rates per unit volume respectively. This equation expresses the conservation of energy. The pressure is the given by the ideal gas equation of state

$$P = (\gamma - 1)\rho u \tag{2.5}$$

where $\gamma$ is the ratio of specific heats.

Rather than using eq. (2.5), for simplicity the barotropic equation of state is used instead to account the transition from isothermal to adiabatic collapse (Boss et al. 2000). It is worth to mention that full and accurate analysis of the evolution of the temperature of the gas structure is achieved including radiative transport coupled to gravity (Whitehouse 2006). The barotropic equation of state reads as follow

$$\frac{P(\boldsymbol{r})}{\rho(\boldsymbol{r})} = c_0^2 \left[1 + \left(\frac{\rho(\boldsymbol{r})}{\rho_{crit}}\right)^{\frac{4}{3}}\right]^{\frac{1}{2}} \tag{2.6}$$

## 2.2 Smoothed Particle Hydrodynamics (SPH)

### 2.2.1 Basic equations of SPH.

Developed by Lucy (1977) and Gingold & Monaghan (1977), SPH is a Lagrangian numerical method that represents the fluid by $N$ discrete particles extended or smoothed over space.

The particles overlap so that the physical quantities involved can be treated as continuous functions in space and time.

The value of any physical variable $A(\boldsymbol{r})$ in the position $\boldsymbol{r}$ is evaluated using

$$A(\boldsymbol{r}) = \sum_i \left\{ \frac{A_i m_i}{\rho_i} h_i^{-3} W\left( \frac{|\boldsymbol{r} - \boldsymbol{r}_i|}{h_i} \right) \right\} \tag{2.7}$$

where $\boldsymbol{r}_i$ is the position, $m_i$ is the mass and $h_i$ is the smoothing length of the particle $i$ (Monaghan & Lattanzio 1985; Monaghan 1988; Monaghan 1992). $A_i$ and $\rho_i$ are the values of $A$ and $\rho$ at $\boldsymbol{r}_i$.

The smoothing function or the kernel $W(r, h)$ describes the intensity and the range of the influence of the particle (Monaghan & Lattanzio 1985; Monaghan 1988; Monaghan 1992)

The kernel 3-D M4 is a polynomial (Springel 2005)

$$W_{M4}(r, h) = \frac{8}{\pi h^3} \begin{cases} 1 - 6\left(\frac{r}{h}\right)^2 + 6\left(\frac{r}{h}\right)^3, & 0 \leq \frac{r}{h} \leq \frac{1}{2}; \\ 2\left(1 - \frac{r}{h}\right)^3, & \frac{1}{2} < \frac{r}{h} \leq 1; \\ 0, & \frac{r}{h} > 1, \end{cases} \tag{2.8}$$

The gradient of any quantity $A$ in a position $\boldsymbol{r}$ is evaluated using

$$\nabla A(\boldsymbol{r}) = \sum_i m_i \frac{A_i}{\rho_i} h_i^{-4} W'\left( \frac{|\boldsymbol{r} - \boldsymbol{r}_i|}{h_i} \right) \frac{\boldsymbol{r} - \boldsymbol{r}_i}{|\boldsymbol{r} - \boldsymbol{r}_i|} \tag{2.9}$$

where $W'(s) \equiv \frac{dW}{ds}$ and $s = \frac{|r|}{h}$ (Monaghan & Lattanzio 1985; Monaghan 1988; Monaghan 1992)

The Continuity equation and the Euler equation, equations (2.1) and (2.2.) in SPH version read as follows

$$\frac{d\rho(\boldsymbol{r})}{dt} = -\rho(\boldsymbol{r}) \sum_i \frac{m_i}{\rho_i} h_i^{-4} v_i \cdot W'\left(\frac{|\boldsymbol{r}-\boldsymbol{r}_i|}{h_i}\right) \frac{\boldsymbol{r}-\boldsymbol{r}_i}{|\boldsymbol{r}-\boldsymbol{r}_i|} \qquad (2.10)$$

where $\rho(\boldsymbol{r}) = \sum_i \left\{ m_i h_i^{-3} W\left(\frac{|\boldsymbol{r}-\boldsymbol{r}_i|}{h_i}\right) \right\}$ from the original definition

and

$$\frac{dv(\boldsymbol{r})}{dt} = -\frac{1}{\rho(\boldsymbol{r})} \sum_i m_i \frac{P_i}{\rho_i} h_i^{-4} W'\left(\frac{|\boldsymbol{r}-\boldsymbol{r}_i|}{h_i}\right) \frac{\boldsymbol{r}-\boldsymbol{r}_i}{|\boldsymbol{r}-\boldsymbol{r}_i|} + \boldsymbol{a}_{grav}(\boldsymbol{r}) + \boldsymbol{a}_{visc}(\boldsymbol{r}) \qquad (2.11)$$

where $\boldsymbol{a}_{visc}$ is the acceleration due to the artificial viscosity (Monaghan 1992)

$$\boldsymbol{a}_{visc}(\boldsymbol{r}) = \sum_i m_i \bar{h}_{ij}^{-4} \Pi_{ij} W'\left(\frac{|\boldsymbol{r}_{ij}|}{\bar{h}_{ij}}\right) \frac{\boldsymbol{r}_{ij}}{|\boldsymbol{r}_{ij}|} \qquad (2.12)$$

$$\Pi_{ij} = \begin{cases} \dfrac{-\alpha \mu_{ij} \bar{c}_{ij} + \beta \mu_{ij}^2}{\bar{\rho}_{ij}}, & (\boldsymbol{v}_{ij} \cdot \boldsymbol{r}_{ij}) < 0; \\ 0, & (\boldsymbol{v}_{ij} \cdot \boldsymbol{r}_{ij}) > 0; \end{cases} \qquad (2.13)$$

$$\mu_{ij} = \frac{(\boldsymbol{v}_{ij} \cdot \boldsymbol{r}_{ij}) \bar{h}_{ij}}{|\boldsymbol{r}_{ij}|^2 + 0.01 \bar{h}_{ij}^2} \qquad (2.14)$$

where $\bar{\rho}_{ij} = 0.5(\rho_i + \rho_j)$ y $\bar{c}_{ij} = 0.5(c_i + c_j)$ is the average sound speed. The strength of the viscosity is regulated by the parameters $\alpha$ and $\beta$, with typical values in the range $\alpha \cong 0.5 - 1.0$ and the frequent choice of $\beta = 1/2 \times \alpha$ (Springel 2005).

Given that the gas is modelled as an ideal gas, shocks or discontinuities may be present within giving artificial effects on the gas. An artificial viscosity term is added to the equations of motion to alleviate this phenomenon.

To reduce the truncation error by the use of equation (2.7), identities used are (Kitsionas 2003)

$$\rho \nabla A = \nabla(\rho A) - A \nabla \rho$$

$$\frac{\nabla A}{\rho} = \nabla \left(\frac{A}{\rho}\right) + \frac{A}{\rho^2} \nabla \rho$$

leading to

$$\rho \nabla \cdot v = \nabla(\rho v) - v \cdot \nabla \rho$$

$$\frac{\nabla P}{\rho} = \nabla \left(\frac{P}{\rho}\right) + \frac{P}{\rho^2} \nabla \rho \tag{2.15}$$

The final SPH equations for the evolution of the hydrodynamical properties are

$$\frac{d\rho(\boldsymbol{r})}{dt} = \sum_i m_i h_i^{-4} (\boldsymbol{v}(\boldsymbol{r}) - \boldsymbol{v}_i) \cdot W' \left(\frac{|\boldsymbol{r} - \boldsymbol{r}_i|}{h_i}\right) \frac{\boldsymbol{r} - \boldsymbol{r}_i}{|\boldsymbol{r} - \boldsymbol{r}_i|} \tag{2.16}$$

$$\frac{d\boldsymbol{v}(\boldsymbol{r})}{dt} = -\sum_i m_i h_i^{-4} \left(\frac{P_i}{\rho_i^2} + \frac{P(\boldsymbol{r})}{\rho(\boldsymbol{r})^2}\right) W' \left(\frac{|\boldsymbol{r} - \boldsymbol{r}_i|}{h_i}\right) \frac{\boldsymbol{r} - \boldsymbol{r}_i}{|\boldsymbol{r} - \boldsymbol{r}_i|} + \boldsymbol{a}_{grav}(\boldsymbol{r}) + \boldsymbol{a}_{visc}(\boldsymbol{r}) \tag{2.17}$$

with the barotropic equation of state

$$\frac{P(\boldsymbol{r})}{\rho(\boldsymbol{r})} = c_0^2 \left[1 + \left(\frac{\rho(\boldsymbol{r})}{\rho_0}\right)^{\frac{4}{3}}\right]^{\frac{1}{2}} \tag{2.18}$$

### 2.2.2 Smoothing and Softening lengths

The smoothing function or the kernel depicted in eq. (2.8) describes the intensity and the range of the influence of the particle and is spline-softened defining a range of influence spherically symmetric. Its compact support makes the particle have a limited number of neighbour particles.

The range of influence is denoted by the smoothing length $h$, so within the smoothing length, the mass of the volume enclosed is kept constant, i.e. the smoothing lengths and the estimated densities obey the (implicit) equations

$$\frac{4\pi}{3}h_i^3\rho_i = N_{sph}\bar{m} \tag{2.19}$$

For each particle $i$, $h_i$ evolves in each timestep, so this is an adaptive smoothing length.

The gravitational softening length $\epsilon_i$ of each particle defines the minimum length of gravitational influence of an SPH particle. The hydrodynamical forces are smoothed at a scale similar to the gravity softening, $\epsilon_i = h_i$. If $\epsilon_i < h_i$ then artificial fragmentation is induced, while for $\epsilon_i > h_i$ fragmentation is inhibited (Bate & Burkert 1997).

## 2.3 The Gadget2 Code

The evolution of the systems to be presented in Chapter 3 is performed by Gadget2 which uses the numerical method SPH, for solving the equations of self-gravitational hydrodynamics and the treePM method for calculating the gravitational forces.

In this section the TreePM method will be described so as the integration schemes that Gadget2 uses to solve the equations for gravitational collapse formulated with SPH.

### *2.3.1 Gravitational algorithms*

### *2.3.1.1 The tree algorithm*

To obtain the required spatial adaptivity, Gadget2 uses a hierarchical multipole expansion called a tree algorithm. Using this method, the number of partial gravitational forces per particle that ranges from $N - 1$ in a direct summation approach is reduced to $O(logN)$. The hierarchical grouping, in the approach of Barnes & Hut (1986), is obtained by recursive subdivision of space starting from a cubic root node or primary node, that encompasses the total mass distribution. This is subdivided into eight sub nodes with half the side-length each of the previous node and so until one reaches the "leaves" where the particles are located, Fig 2.1. So as one goes to smaller scales the tree is traveled along to arrive at the partition where there is just one particle. The accuracy of the method consists of how below the primary node or "the tree root" is traveled and this means how accurate the gravity forces are calculated. As a result, the final forces are only an approximation to the true force. However, the error can be controlled conveniently by modifying the opening criterion for the tree nodes.

Provided sufficient computational resources are invested, the tree force can then be made arbitrarily close to the well-specified correct force.
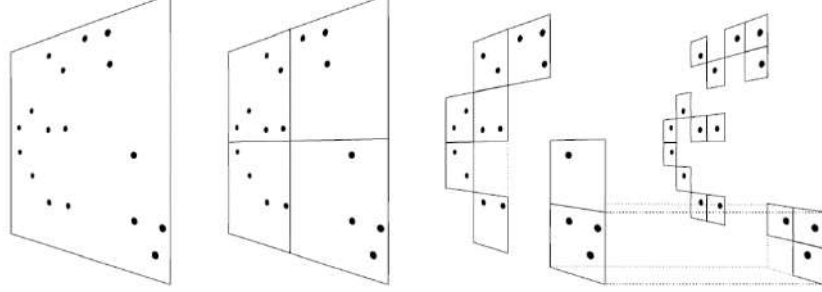


Fig. 2. 1. "Schematic illustration of the Barnes & Hut oct-tree in two dimensions. The particles are first enclosed in a square (root node). This square is then iteratively subdivided in four squares of half the size, until exactly one particle is left in each final square (leaves of the tree). In the resulting tree structure, each square can be progenitor of up to four siblings. Note that empty squares need not to be stored". Image retrieved from Springel, V., Yoshida, N., & White, S. D. (2001). GADGET: a code for collisionless and gas dynamical cosmological simulations. *New Astronomy*, *6*(2), 79-117.

### 2.3.1.2 TreePM method

The treePM method is constructed as a hybrid method of the particle-mesh method and the tree algorithm (Bagla 2002). The gravitational potential is explicitly split in Fourier space into long-range and short-range parts according to $\phi_k = \phi_k^{long} + \phi_k^{sh}$ where

$$\phi_k^{long} = \phi_k \exp(-k^2 r_s^2) \tag{2.20}$$

with $r_s$ describing the spatial scale of the force-split. According to Springel (2005), the $\phi_k^{long}$ can be computed very efficiently with mesh-based Fourier methods. If $r_s$ is chosen slightly larger than the mesh scale, force anisotropies that exist in plain PM methods can be suppressed to arbitrarily small levels.

The short part of the potential can be solved in real space. For $r_s \ll L$, the short-range part of the solution for the potential is

$$\phi(x)_k^{sh} = -G \sum_i \frac{m_i}{r_i} \text{erfc}\left(\frac{r_i}{2r_s}\right) \tag{2.21}$$

Here $r_i = min(|x - r_i - nL|)$ is defined as the smallest distance of any of the images of particle $i$ to point $x$. Because the complementary error function rapidly suppresses the force for distances large compared to $r_s$ (the forces drop to about 1% of its Newtonian value for $r \cong 4.5r_s$), only this nearest image has any chance to contribute to the short-range force.

Now, with eq. (2.21) the force is computed by the tree algorithm with a short-range cut-off factor modification of the law force.

### 2.3.2 Quasi-Symplectic Time Integration

#### 2.3.2.1 The symplectic nature of leapfrog

Gadget2 uses an integration scheme of symplectic nature given that traditional methods like Runge-Kutta introduces non-Hamiltonian perturbations that affect the long term behaviour of the solutions. Using a symplectic approach, the Hamiltoninan structure of the system is preserved by formulating each step as a canonical transformation, leaving invariant the symplectic two-form of the Hamiltonian, eliminating perturbations and leaving the system stable.

The Hamiltonian of the usual N-body problem can be separable in the form

$$H = H_{kin} + H_{pot} + H_{therm} \tag{2.22}$$

where the thermal energy part is given by

$$H_{them} = \frac{1}{\gamma - 1} \sum_i m_i A_i \rho_i^{\gamma - 1} \tag{2.23}$$

For this case, the time-evolution operators $D_t(\Delta t)$ and $K_t(\Delta t)$ for each part of the Hamiltonian can be computed exactly. The drift and kick operators (Springel 2005 and references therein) are given by

$$D_t(\Delta t): \begin{cases} p_i & \mapsto & p_i \\ x_i & \mapsto & x_i + \frac{p_i}{m_i} \int_t^{t+\Delta t} \frac{dt}{a^2} \end{cases} \tag{2.24}$$

$$K_t(\Delta t): \begin{cases} x_i & \mapsto & x_i \\ p_i & \mapsto & p + f_i \int_t^{t+\Delta t} \dfrac{dt}{a^2} \end{cases} \tag{2.25}$$

where $f_i = -\sum_j m_i m_j \frac{\partial \phi(x_{ij})}{\partial x_i}$ is the force on particle i. Both $D_t$ and $K_t$ are symplectic operators because they are exact solutions for arbitrary $\Delta t$ for the canonical transformations generated by the corresponding Hamiltonians. From this, it can be derived a time evolution operator $U(\Delta t)$ for an interval $\Delta t$

$$\widetilde{U}(\Delta t) = D\left(\frac{\Delta t}{2}\right) K(\Delta t) D\left(\frac{\Delta t}{2}\right) \tag{2.26}$$

or

$$\widetilde{U}(\Delta t) = K\left(\frac{\Delta t}{2}\right) D(\Delta t) K\left(\frac{\Delta t}{2}\right) \tag{2.27}$$

which correspond to the drift-kick-drift (DKD) and kick-drift-kick (KDK) leapfrog integrators. Both of these integration schemes are symplectic, because they are a succession of symplectic phase-space transformations. In fact, $\widetilde{U}$ generates the exact time evolution of a modified Hamiltonian $\widetilde{H}$. Writing $\widetilde{H} = H + H_{err}$, one finds (Springel 2005 and references therein)

$$H_{err} = \frac{\Delta t^2}{12} \left\{ \{H_{kin}, H_{pot}\}, H_{kin} + \frac{1}{2} H_{pot} \right\} + \mathcal{O}(\Delta t^4) \tag{2.28}$$

*2.3.2.2 Individual and adaptive timesteps*

In the simulations performed in this work, there is a large dynamic range in timescales. In high density regions, smaller timesteps are required than in lower-density regions. Evolving all particles with the smallest required timestep hence implies a substantial waste of computational resources. An integration scheme with individual timesteps deals with this situation more efficiently. The main idea is to compute forces only for a certain group of particles in a given kick operation, with the other particles being evolved on larger timesteps.

Unfortunately, formal symplectic integration for individual timesteps is not possible given that the potential part of the Hamiltonian is not separable. However, the potential between two particles can be partitioned into a long-range and short-range part, as in the treePM algorithm. This leads to a separation of the potential part of the Hamiltonian into

$$H_{pot} = H_{sr} + H_{lr} \tag{2.29}$$

Now the symplectic integrators can be obtained by subcycling the evolution under $H_{kin} + H_{sr}$ (Springel 2005 and references therein). For example

$$\tilde{U}(\Delta t) = K_{lr}\left(\frac{\Delta t}{2}\right)\left[K_{sr}\left(\frac{\Delta t}{2m}\right)D\left(\frac{\Delta t}{m}\right)K_{sr}\left(\frac{\Delta t}{2m}\right)\right]^m K_{lr}\left(\frac{\Delta t}{2}\right) \tag{2.30}$$

where $m$ is an integer. This is the scheme Gadget2 uses for integration with the treePM algorithm. The long-range PM force has a comparatively large timestep, which is sufficient for the slow time-variation. This force is calculated for all the particles. For the short-range part, which varies on shorter timescales, is done on a power of 2 subdivided timescale.

## 2.4 The Particle Splitting Technique

### 2.4.1 Concept

As the core evolves under gravitational collapse, the local maximum density peak increases and the condition $M_0 > M_J$, where $M_0$ is the mass of a proto-condensation and $M_J$ is the Jeans mass, is quite satisfied, meaning that it is unstable against collapse. Also, as the requirement $M_{min} < M_j$ , where $M_{min}$ is the minimum resolvable mass and is given by $M_{min} = N_{neig}m_{SPH}$, is satisfied, artificial fragmentation is inhibited, and no spurious perturbations contaminate the solution. As long as $M_0 >> M_{min}$, the proto condensation is well resolved so the simulation evolves correctly showing all the features of the structures within the core. However, as the system evolves, the mass of the proto-condensation will eventually be smaller than the minimum resolvable mass $M_0 << M_{min}$ and the simulation will not have adequate resolution anymore. Clearly one must reduce $M_{min}$ to get the requirement satisfied. This translates to reducing the minimum resolvable mass and increasing the number of SPH particles. Kitsionas and Whitworth (2002) developed a method that replaces individual, or

*parent particles* from now on, for families of finer particles, or *children particles*, distributed according to a specific geometry. In this manner, the masses of individual particles are reduced, and the number of particles is increased on regions where resolution is not adequate, or an improved resolution is desired. For their case, each children particle has a mass $m_{child} = m_{parent}/13$.

In standard SPH, the range of an individual particle smooths or extends over a spherically symmetric geometry by virtue of its smoothing length. This means that the particles should be distributed so that the sum of the smoothing lengths of the children particles approximately preserves its spherical symmetry.

Children particles are placed on a specific close-packed configuration. In their study, Kitsionas & Whitworth (2002) used a configuration with hexagonal geometry placing one child particle in the position of the parent particle and the rest of the children particles located upon the surface of the hexagonal array at a distance $\ell$ from the child particle in the center. They used a set of 13 new particles taking the following considerations: 1) There should not be too large difference between the mass of a parent particle and the children particles, otherwise large numerical diffusion may be present whenever parent and children particles are neighbours and 2) The variance in the density profile of parent particles and the collective density of children particle should be relatively small.

### 2.4.2 Nested Splitting

One way of implementing particle splitting is nested splitting, which consists on starting a standard simulation at $t = 0$ and then at $t_{split}$ $(> 0)$ identify a subdomain where improvement on the resolution is required. Then all particles on this subdomain are split. The velocity of children particles is calculated from the contributions of the ~50 neighbours of - and including- the parent particle (index $i$) (Kitsionas & Whitworth 2002):

$$\boldsymbol{v}_{i'} = \sum_j \left\{ \frac{m_j \boldsymbol{v}_j}{\rho_j \bar{h}_{ij}^3} W \left( \frac{|\boldsymbol{r}_{i'} - \boldsymbol{r}_j|}{h_{ij}} \right) \right\} \tag{2.31}$$

After $t_{split}$ any parent particle that enters the subdomain is immediately split and the resulting fine child particles are again given the velocities by summing over the neighbours of the parent particle. Better results are obtained if the total mass of neighbour particles is ~50 times the total mass of the parent particle, instead of requiring the number of neighbours to be ~50.

### 2.4.3 On-the-fly Splitting

This version of particle splitting identifies particles with insufficient resolution for the problem in hand and split them as the simulation evolves the system. This is obtained by computing the minimum resolution requirement via the Jeans condition, described in section 2.2.3, for a region of interest and trigger particles splitting once the threshold density is reached. Then, velocities for the children particles are evaluated using the same equation as in nested slitting.

### 2.4.4 The unit cell

As mentioned earlier, when particle splitting is applied, a parent particle is substituted by an array of children particles with a specific geometry. The problem of distributing a given number of particles uniformly over a surface has been considered by mathematicians since long time ago (Staff and Kuijlaars et al., 1997) and today is still a matter of active research (Raskin and Owen, 2016).

For this reason, there can be many useful choices of geometric arrays for the unit cell. For the present work, it is considered a unit cell with the geometric array of the zinc sulfide molecule with eighteen child particles, which is shown in fig 2.4. Two colors have been used to illustrate the particles within the unit cell; green squares represent interior particles and blank circles the exterior ones. The codes for generating the unit cells are written in ANSI C programming language.

It should be mentioned that 1) before the unit cell is loaded to replace the parent particles in the code, its orientation is modified by applying random rotations about the geometric center, so the axis of symmetry points to an arbitrary direction; 2) in addition, in fig 2.5 the cell length is in arbitrary units. When the unit cell is implemented, it takes the real value to make the calculations by Gadget2.
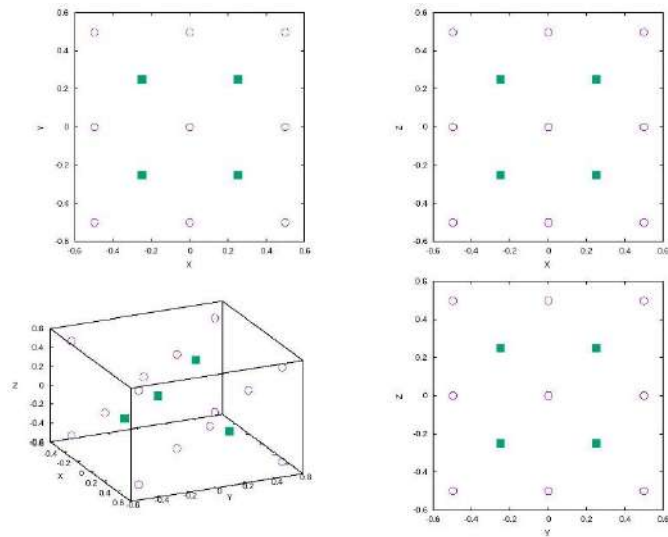
Fig. 2. 2. Zinc sulfide unit cell. Interior particles in green squares and exterior particles in blank circles.

# Chapter 3 – The Physical Systems

In this chapter, the physical systems are presented just as the procedure of implementation of particle splitting on the initial conditions. The idea is to replace the original particles of the simulation with unit cells so that resolution is improved on regions of interest. But first, a trial model is developed mainly for visualization purposes so one can have a look of what the unit cell looks like in a uniform grid, making adjustments of the length of the unit cell, which will take the role of the SPH smoothing length $h$, to see how the finer particles readjust their distances from each other. This length adjustment is also for purposes of visualizing the effect of a variable smoothing length.

The simulations are based on two physical systems: a gas core with rigid-body rotation and a turbulent core. For the original simulations, these are named *base models* and the simulations with particle splitting using the unit cell are named *modified simulations*. The calculations are performed with Gadget2.

## 3.1 Trial model

A trial model is worked out to take an insight on the process of the implementation of the unit cell. This model consists of a system of particles positioned uniformly upon a cartesian grid generated in a three-dimensional space region. The original particles are replaced by the unit cells and are distributed uniformly. Once they are at their final positions, they are rotated in random directions.

### 3.1.1 Generation of the uniform grid

This grid consists of points equally spaced by a unit length and particles are positioned upon them. This can be generated for both the whole computational region and for the region of a

single particle when the unit cell is implemented. These are shown in fig. 3.1 and 3.2, respectively. The implementation of the unit cell in three-dimension and XY two-dimension views is shown in fig. 3.3 and in fig. 3.4, XY two-dimension views of the unit cell with various values for the cell length $h$.
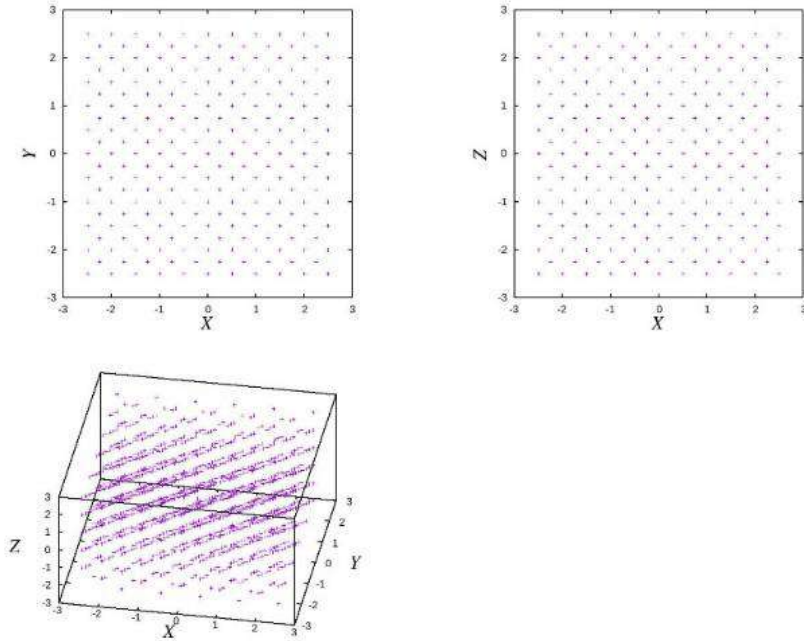
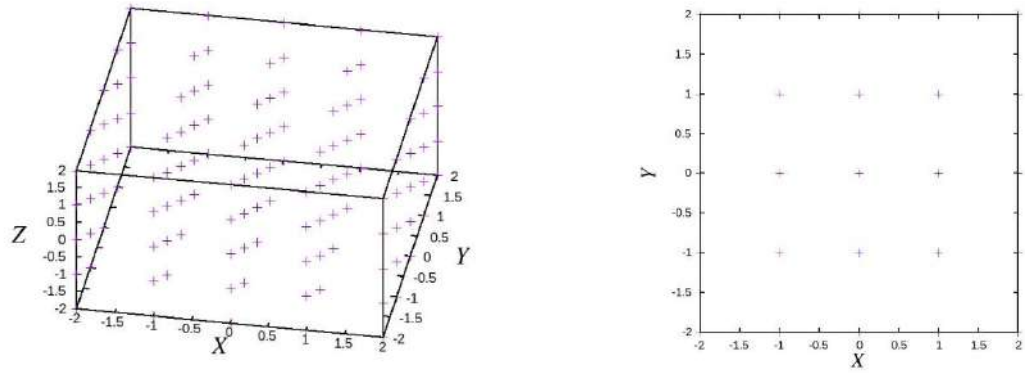

Fig. 3. 1. Uniform grid from XY, XZ and 3D views.

Fig. 3. 2. Uniform grid for a unit cell in XY and 3D views.
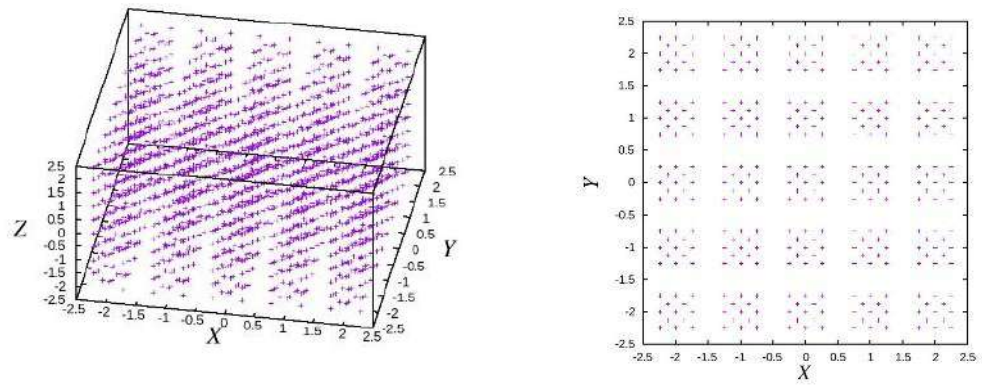


Fig. 3. 3. Uniform grid with unit cells implemented in XY and 3D views.
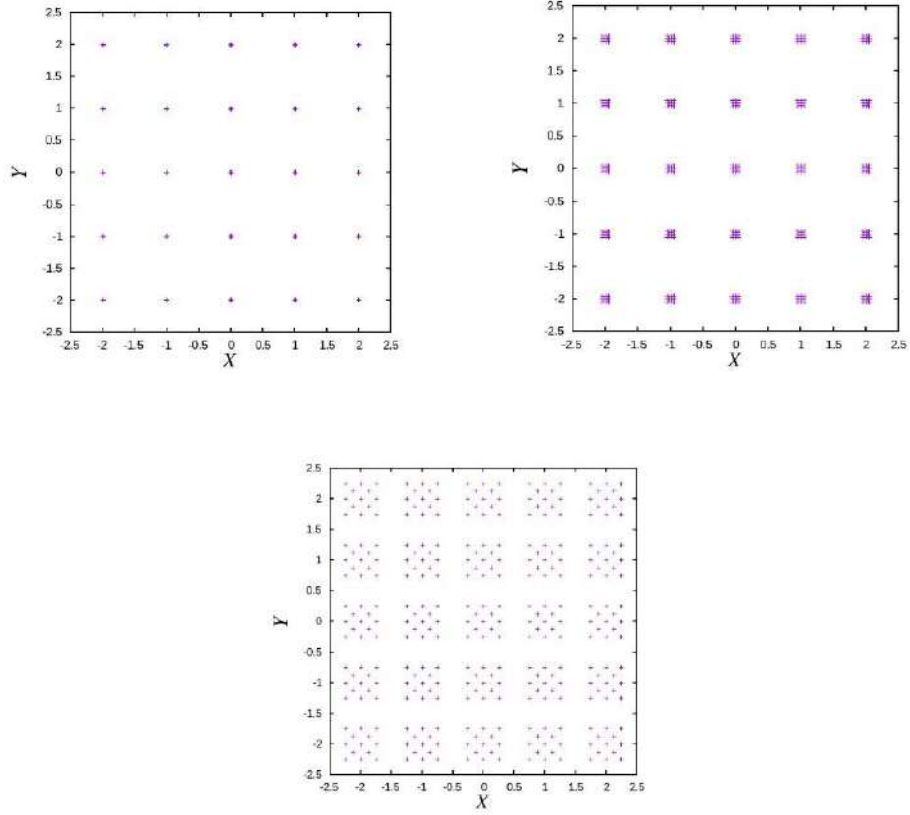
Fig. 3. 4. Uniform grid with different values of h of the unit cell. Top left h=0.01, top right h=0.1, bottom h=0.5.

### 3.1.2 Eulerian rotations

To get the child particles in their final positions, random rotations on each unit cell are performed about the three Eulerian angles $\theta, \phi$ and $\psi$, fig 3.5 (Goldstein 2002). This ensures no special or defined order in the arrangements that might affect the results directly. The rotation matrix reads

$$A = \begin{bmatrix} cos\psi cos\phi - cos\theta sin\phi sin\psi & cos\psi sin\phi + cos\theta cos\phi sin\psi & sin\psi sin\theta \\ -sin\psi cos\phi - cos\theta sin\phi cos\psi & -sin\psi sin\phi + cos\theta cos\phi cos\psi & cos\psi sin\theta \\ sin\theta sin\phi & -sin\theta cos\phi & cos\theta \end{bmatrix} \quad (3.1)$$

where the angles $\theta, \phi, \psi$ correspond to the ones shown if fig. 3.5.

Fig. 3. 5. Rotation about Eulerian angles. Adapted from Goldstein, H., Poole, C., & Safko, J. (2002). Classical mechanics.

In figs. 3.6 and 3.7 are shown the configuration of the unit cells as rotated by a small amount about each Eulerian angle and by an arbitrary amount of rotation, respectively.
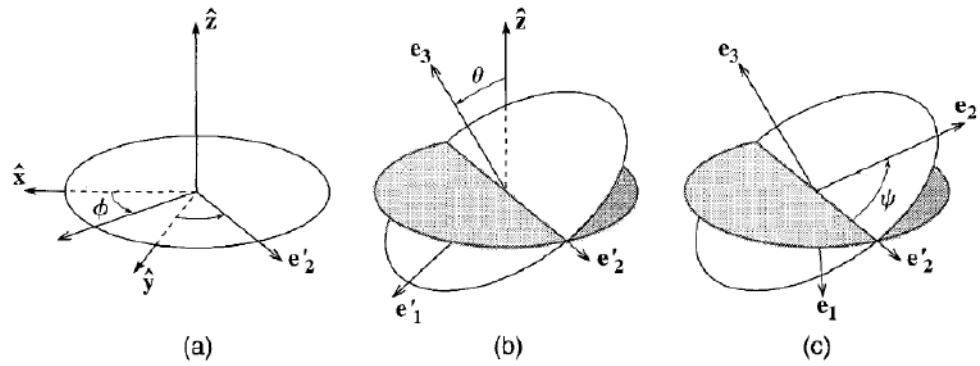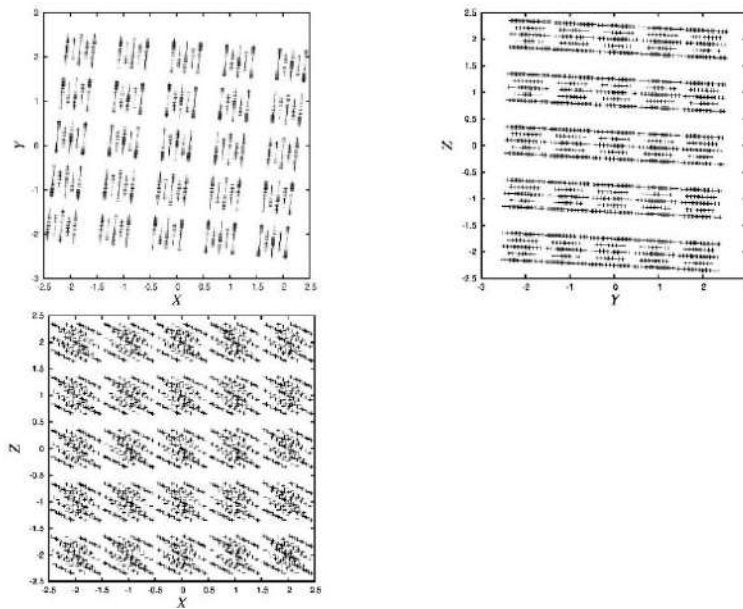


Fig. 3. 6. Uniform grid with unit cells rotated by a small amount about the Eulerian angles.
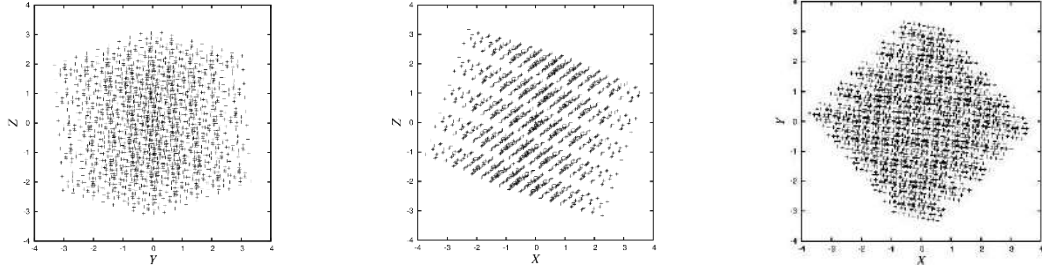
Fig. 3. 7. Uniform grid with unit cells rotated arbitrarily about the Eulerian angles.

## 3.2 Simulation of the Physical Systems

### 3.2.1 The gas core

The initial physical parameters for the models here studied are as follows: Initial radius of the core $R_0 = 2.99 \times 10^{17} cm \equiv 0.097 \, pc$, total mass $8 \, M_{\odot}$, average density given by $\rho_0 = 1.4 \times 10^{-19} \text{g cm}^{-3}$. A test particle, affected only by the gravitational force of this core, will reach the core center in a time given by $t_{ff} = \sqrt{\frac{3\pi}{32G_{\rho_0}}} = 177.6 \, kyr$ (kilo $-$ years $= 10^3$ years), which is the free-fall time $t_{ff}$. G is Newton's gravitational constant.

The number density of both gas cores is $n_0 = 41916$ particles per $\text{cm}^3$. It should be emphasized that these physical properties are typical of cores, in statistical terms, see for instance (Jijina et al. 1999) and (Bergin et al. 2007) and are similar to the properties of the well-studied dense core L1544, see (Tafalla et al. 2004). These authors have presented evidence indicating that the core L1544 is collapsing towards one or two low-mass stellar system. In addition, Goodwin et al. (2004a) considered simulations of the core L1544 by means of turbulent models.

For the simulations here performed there are two main dynamical models: A core with rigid-body rotation and a core with induced turbulence. The core with rigid-body rotation has been studied for a long time and it is included on this work as a reference to compare the performance of the codes here developed. One of the most relevant studies of this system was done by Kitsionas and Whitworth (2002) using SPH and the particle splitting technique. They

31

applied the technique to a relatively small number of particles, those that needed an enhancement of resolution. The outcome of the simulation is the well-known thin, long filament of dense particles with two cloudlets at both extremes of the filament.

On the other hand, the gas cores with induced turbulence have called the attention of many authors since turbulence appears to be responsible of much of the structures and formations observed in molecular clouds at various scales. When turbulence is continuously replenished in the large-scale, global collapse is prevented (Dubinski et al. 1995; Offner et al. 2008). For this work, turbulence is induced only at the initial time of the collapse so one can expect the turbulence to dissipate at a relatively early stage and the process of collapse to take place freely giving as an outcome a single protostellar object at the end of the simulation.

### 3.2.2 The initial position of the particles

The volume in which the simulation takes place is partitioned in a 3D- mesh $\Delta x$, $\Delta y$, $\Delta z$. The initial position of each particle is at the center of this small cubic element. Once the particle is positioned, it is given a displacement of $\Delta/4$ in random spatial directions within each cubic element.

The mass of each particle is given by the initial density $\rho_0$ so that the particle $i$ has a mass $m_i = \rho_0 \times \Delta x \Delta y \Delta z$ for $i =1,\ldots,996972$ the total number of particle for the base simulation.

For the turbulent core, all the simulation particles have the same mass. However, in the case of the rotating core, a perturbation is needed in order to start the collapse with a seed of a binary system. This work follows (Springel 2005), so that this seed is achieved by means of a mass perturbation of the form

$$\delta m_i = m_i \times acos(m_i \emptyset_i) \tag{3.2}$$

where the perturbation amplitude $a$ is set to $a =0.1$ and the mode is fixed to $m =2$.

### 3.2.3 The initial velocities of the particles

The initial velocity for the particle $i$ in the rotating model is given by

$$v_i = \Omega \times r_i \tag{3.3}$$

where $\Omega$ is the angular velocity of the particle $i$ and has the magnitude of $1.15\times10^{-13}$ rad/s. It is assumed that the rotation is about the z-axis, so the initial velocity is given by $(-\Omega y_i, \Omega x_i, 0)$. This angular velocity has been chosen to satisfy the energy requirement described before.

For the turbulent core, the velocity vector of a particle is a linear combination of Fourier modes, which are populated in a 3D-cubic mesh with $N_g$ grid elements per side. Each Fourier mode has the components $\left(i_{K_x}\delta K_x, i_{K_y}\delta K_y, i_{K_z}\delta K_z\right)$ where the indices $i_{K_x}$, $i_{K_y}$, $i_{K_z}$ take values on the interval $\left[-N_g/2, N_g/2\right]$ and $\delta K_x = \delta K_y = \delta K_z = 1.0/R_0$.

According to Dobbs et al. (2005) the velocity of the particle $i$ is

$$v \approx \sum_{i_x i_y i_z} |K|^{\frac{n-2}{2}} \times \begin{cases} \left[K_z C_{K_y}\sin\left(K\cdot r + \Phi_{K_y}\right) - K_y C_{K_z}\sin(K\cdot r + \Phi_{K_z})\right] \text{ for } v_x \\ \left[K_x C_{K_z}\sin(K\cdot r + \Phi_{K_z}) + K_z C_{Kx}\sin(K\cdot r + \Phi_{K_x})\right] \text{ for } v_y \\ \left[K_x C_{K_y}\sin\left(K\cdot r + \Phi_{K_y}\right) + K_y C_{K_x}\sin(K\cdot r + \Phi_{K_x})\right] \text{ for } v_z \end{cases} \tag{3.4}$$

where the spectral index $n$ is fixed as $n = 1$ and thus we have $v^2 \approx K^{-3}$

The vector $C$ whose components are denoted by, $\left(C_{k_x}, C_{k_y}, C_{k_z}\right)$ take values on a Rayleigh distribution. The wave phase vector, $\Phi$, given by $\left(\Phi_x, \Phi_y, \Phi_z\right)$ takes random values on the interval $[0, 2\pi]$. The vector $C$ components are calculated by means of $C = \sigma \times \sqrt{-2.0 \times \log(1.0 - u)}$ where $u$ is a random number in $(0,1)$. $\sigma$ is a fixed parameter with value 1.0. The level of kinetic energy can be adjusted simply by multiplying in front of the right-hand side of eq. (3.4) by a constant, which must be done in order to satisfy the energy ratios to be defined in section 3.2.4.

### 3.2.4 Initial energies

To be able to make a useful comparison of the output of all the models, the relevant energy ratios have been calculated to be the same in all the models, as follows. The relevant energies are:

$$E_{ther} = \frac{3}{2} \sum_i m_i \frac{P_i}{\rho_i}$$

$$E_{kin} = \frac{1}{2} \sum_i m_i v_i^2 \tag{3.5}$$

$$E_{grav} = \frac{1}{2} \sum_i m_i \Phi_i$$

where $P_i$ and $\Phi_i$ are the pressure and gravitational potential for particle $i$, with velocity $v_i$ and mass $m_i$. The summations in Eq. (3.5) must include all the simulation particles of the simulation.

In this work, the value of the speed of sound $c_s = 15{,}230$ cm/s is chosen in each model so that the simulations have

$$\alpha \equiv \frac{E_{ther}}{|E_{grav}|} = 0.16 \tag{3.6}$$

It should be noticed that there are many values of this ratio used in the literature, for instance, (Goodwin et al 2004a) used a value of $\alpha = 0.45$.

The level of kinetic energy is chosen for all the simulations to have

$$\beta \equiv \frac{E_{kin}}{|E_{grav}|} = 0.10 \tag{3.7}$$

Later, the virial theorem will be useful to show the level of virializations of the simulation output; in term of the energy ratios defined in Eqs (3.5) and (3.6)

$$\alpha + \beta < \frac{1}{2} \tag{3.8}$$

It is expected that if a gaseous system has $\alpha + \beta > \frac{1}{2}$, then it will expand; in the other case, if $\alpha + \beta < \frac{1}{2}$, then the system will collapse.

## 3.3 The models and implementation of particle splitting

The approach taken in this work is somewhat different from the ones developed by Kitsionas & Whitworth (2002). The first version is by applying particle splitting over all the particles of the base simulation at time $t = 0$ so all parent particles are replaced by children particles using the unit cell from the beginning of the simulation. Here the increase of resolution is global. The second version is by applying particle splitting on a subset of parent particles, those that are before-hand known to reach a given threshold density at the end of the base simulation. All simulations with no particle splitting applied are given the name of *base simulations*, and simulations with particle splitting, *modified simulations.* For the modified simulations with particle splitting applied globally, they are labeled with superscript (a) and for the modified simulations applied to a subset of parent particles, they are labeled with superscript (s). In this work are considered two systems; a uniform rigid-body rotational core, with label R and a turbulent core with label T. Base and modified simulations are shown in table 1.

The most important parameters in the implementation of the particle splitting technique are: First, the unit cell length, which is taken as the smoothing length $h$ and it is calculated by Gadget2 for each particle in both the base and modified simulations in each timestep.

The second parameter is the number of new gas particles associated with each parent particle, which are called children particles, $N_C$. This parameter determines the mass of a child particle, which is given by $m_{child} = m_{parent}/N_c$, where $m_{parent} = m_i$, and $m_i$ is defined in section 2.4. Thus, the total mass of the base simulation does not change when additional children particles are created.

The third parameter is the number of particles of the base simulation upon which particle splitting is applied, and it is denoted here by $N_{Res}$, see column four in table 1. When all particles are affected by the technique, improvement of resolution is global, and simulation takes the label superscript (a). When the technique is applied to a subset of particles, improvement of resolution is localized, and the simulation takes the label superscript (s).

| Model | Label | $N_{Res}$ | $N_T$ | $t_{max}/t_{ff}$ | $log_{10}(\rho_{max}/\rho_0)$ |
|---|---|---|---|---|---|
| 1 | $R$ | 0 | 996,972 | 1.27 | 8.43 |
| 2 | $ResR\,{}_z^a$ | 996,972 | 17,945,496 | 0.97 | 7.99 |
| 3 | $ResR\,{}_z^s$ | 192,584 | 4,270,899 | 1.06 | 7.97 |
| 4 | $T$ | 0 | 996,972 | 1.10 | 9.46 |
| 5 | $ResT\,{}_z^a$ | 996,972 | 17,945,496 | 1.06 | 8.80 |
| 6 | $ResT\,{}_z^s$ | 291,671 | 5,955,378 | 1.09 | 4.77 |

Table 3. 1. The models

# Chapter 4 - Results

In this chapter, the results of the simulations with the imposed initial conditions described in Chapter 3 are discussed. The plots shown in the following sections are slices at the equator of the core that show the density distribution and are shown at initial time, when the core is about to begin the process of collapse, and at final time when the core reaches a pre-defined density value. All plots show, unless otherwise specified, in their left panels the models with particle splitting applied to all the particles in the core with superscript (a), and in the right panels, the particle splitting technique applied to a subset of particles those that reach a threshold value given at the end of the base simulations, with superscript (s). It is worth mentioning that the values of the scale bars have been lowered from the real density values to have a better visualization of the plots and ease the comparison between different models.

The time evolution of the models was carried out with the Ocotillo supercomputer of the Area de Computo de Alto Rendimiento (ACARUS) of the Universidad de Sonora running in parallel in 20 processors per model.

## 4.1 Initial configurations

In fig 4.1 are shown density plots of the rotating and turbulent models which corresponds to the left and right panels, respectively. In the case of the rotating model the density distribution can be seen clearly to be originated by an azimuthal perturbation, in this case generating a density enhancement as the one seen in the plot. The turbulent core shows a uniform distribution with localized density enhancements produced by the velocity turbulence spectrum. Notice that these enhancements on the density form swarms of interconnected pockets of gas.
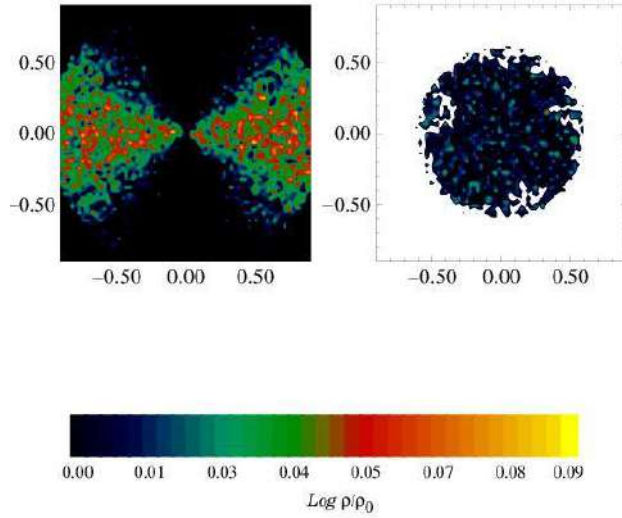
Fig. 4. 1. Initial configuration of the base simulations by means of density plots for a gas slice of the xy-midplane region (-1.0/$R_0$) of the models: Density peak $log_{10}(\rho_{max}/\rho_0) = 0.12$ for the rotating core (left panel); Density peak $log_{10}(\rho_{max}/\rho_0) = 0.09$ for the turbulent core (right panel).

In fig. 4.2 are shown the rotational core models. The core in the left panel shows a uniform density distribution on the whole cross section with a little non-uniformity in the lower right region. The core of the right panel shows an enhancement of density in the regions with particles that reach a given density threshold at the end of the evolution time of the base simulation. These corresponds to the particles affected by the azimuthal perturbation. The void in the upper region may be due to the choice of the length of $h$.
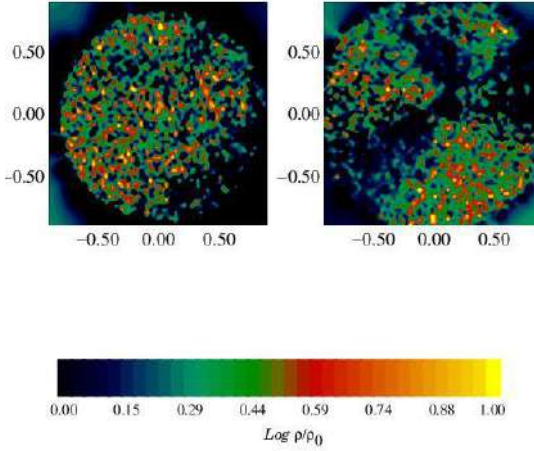
Fig. 4. 2. Initial configuration of the modified simulations ResR[a] and ResR[s] by means of density plots for a gas slice of the xy-midplane region(-1.0/$R_0$) of the models: Density peak $log_{10}(\rho_{max}/\rho_0) = 2.40$ for ResR[a] (left panel); Density peak $log_{10}(\rho_{max}/\rho_0) = 2.62$ for ResR[s] (right panel).

Fig 4.3 shows the turbulent cores. The core in the left panel shows nearly uniform enhancement on the density distribution with density scale higher than the one of the right panel. This is due to particle splitting applied to all particles; the density enhancements are present on the whole cross section of the core. Notice the high-density concentrations across the whole section. In the right panel, the density enhancements are also distributed uniformly on the whole cross section, but this model is affected by particle splitting partially not upon all particles. The density in the clumps is not as high as the one on the left panel. Higher density concentrations are not developed yet as in left panel.
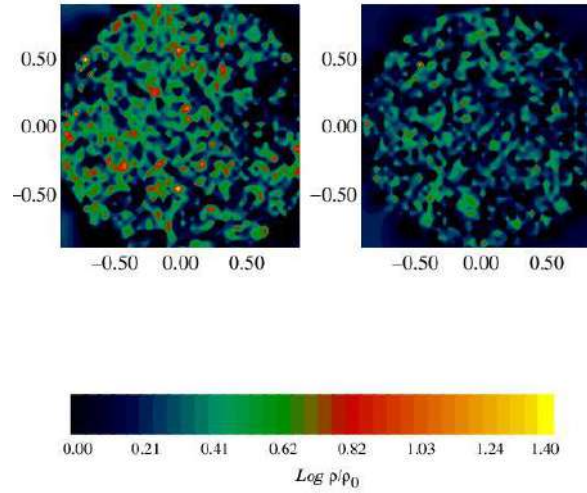
Fig. 4. 3. Initial configuration of the modified simulations ResT[a] and ResT[s] by means of density plots for a gas slice of the xy-midplane region($-1.0/R_0$) of the models: Density peak $log_{10}(\rho_{max}/\rho_0) = 2.55$ for ResT[a] (left panel); Density peak $log_{10}(\rho_{max}/\rho_0) = 2.17$ for ResT[s] (right panel).

## 4.2 Final configurations

In fig. 4.4 are shown the final configurations of the rotating and turbulent core base models. The left panel being the rotating core, shows a system of two cloudlets with a diffuse thin filament bridging them. This result is the one obtained by Boss & Bodenheimer (1979) and many other authors for the standard isothermal cloud collapse. In the left panel, the turbulent core forms a single central condensation.
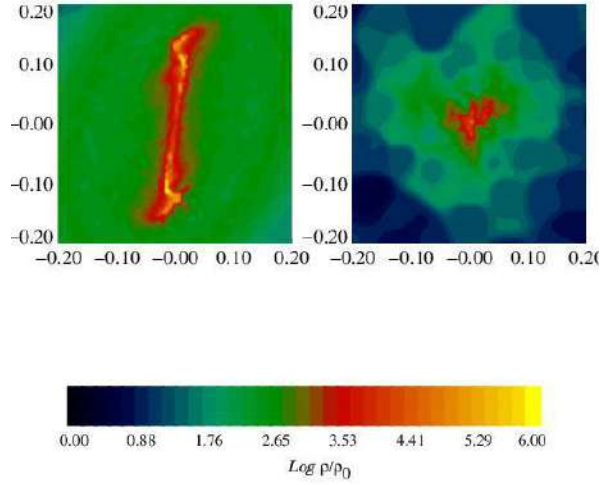
Fig. 4. 4 Final configuration of the base simulation by means of density plots for a gas slice of the xy-midplane region(-1.0/$R_0$) of the models: Density peak $log_{10}(\rho_{max}/\rho_0) = 8.43$ and time $t/t_{ff} = 1.27$ for the rotating core (left panel); Density peak $log_{10}(\rho_{max}/\rho_0) = 9.46$ and time $t/t_{ff} = 1.10$ for the turbulent core (right panel).

In fig. 4.5 are shown the modified simulations for the rotating core. The output which shows the final configurations gives results quiet different from the ones expected. The model ResR[(a)] results in a system of two small condensed arm-like cloudlets with a little thin bar bridging them with substructure within. The model ResR[(s)] also gives two condensed objects almost equally dense than the ones on the left panel but with a shorter bar between them. The substructure observed may be attributed to the enhancement of resolution.

Fig. 4. 5. *Vis a vis* comparison between the ResR[a] and ResR[s] by means of density plots for a gas slice of the xy-midplane region($-1.0/R_0$) of the models: Density peak $log_{10}(\rho_{max}/\rho_0) = 7.99$ and time $t/t_{ff} = 0.97$  for ResR[a]  (left panel); Density peak $log_{10}(\rho_{max}/\rho_0) = 9.46$ and time $t/t_{ff} = 1.10$ for ResR[s] (right panel).

In fig 4.6 are shown the modified simulations of the turbulent models. On both models, the output is the one expected being a single central condensation with substructure. The left panel exhibits an elongated filament. The plot in the right panel exhibits a central clump with two main arms extended at perpendicular directions. These observed substructures are due to the enhancement of the resolution and are consistent with the output of the base simulation.
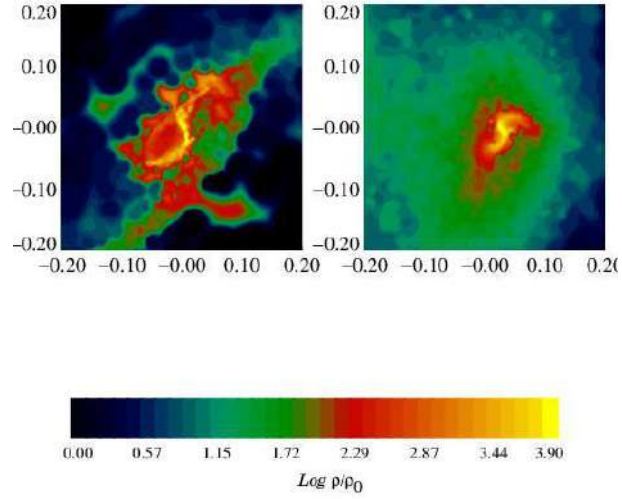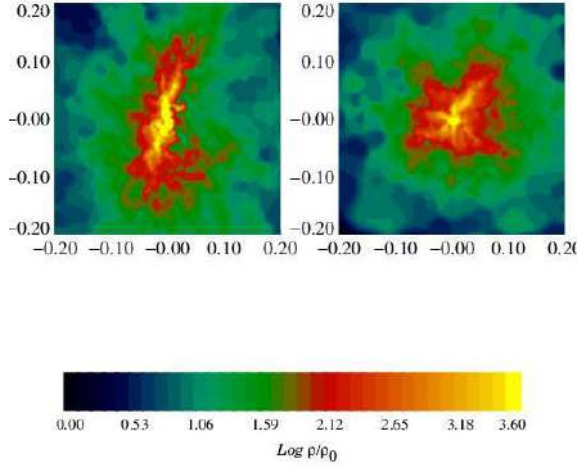
Fig. 4. 6. *Vis a vis* comparison between the ResT[a] and ResT[s] by means of density plots for a gas slice of the xy-midplane region(-1.0/$R_0$) of the models: Density peak $log_{10}(\rho_{max}/\rho_0) = 8.80$ and time $t/t_{ff} = 1.06$ for ResT[a] (left panel); Density peak $log_{10}(\rho_{max}/\rho_0) = 4.77$ and time $t/t_{ff} = 1.09$ for ResT[s] (right panel).

## 4.3 Time evolution of the models

To complement the descriptions given in sections 4.1 and 4.2 about the initial and final configurations of the models, in this section their time evolution is described.

In fig. 4.7 the maximum peak density versus time is plotted, in the left panel for the rotating models, and in the right panel for the turbulent ones. All the modified models, both rotating and turbulent, produce at $t = 0$ an over-density higher than $\rho_0$. This is explained by the fact that particle splitting introduces the new children particles, so this is the first feature one is able to see in the evolution curve. At time $t/t_{ff} \approx 0.10$ on both cores, the peak density reaches a minimum in which the cores undergo a spatial expansion. It should be noticed that the base simulations, on both rotating and turbulent, begin with an initial density $\rho_0$ which experiment no density lowering process.

For the rotating cores, the collapse ends approximately at $t/t_{ff} \approx 0.85$ for the ResR[a] model and $t/t_{ff} \approx 0.95$ for the ResR[s] model. The base model collapse finishes at a time

43

$t/t_{ff} \approx 1.15$. In the case of the turbulent models, all the modified models follow closely the evolution of the base model T up to $t/t_{ff} \approx 1$.

Let us recall that the well-known filament shown in the left panel of fig 4.4 is formed because of the high level of symmetry between the two density perturbations, which are azimuthal antipode of one another. The system with spiral arms bridged with a short bar generated by ResR[a] forms because of the uniform density distribution, originated by the application of the technique over all the particles in the simulation. Here the azimuthal density perturbation is hardly seen also due to the application of the technique. On the other hand, the model ResR[s] presents at initial time, an enhancement in the density with distribution following the azimuthal perturbation. This means that the particles affected by the technique are the ones located in the regions where the perturbation was applied and those that form the system shown in the plot at the final evolution time. It should be highlighted that this model lacks symmetry, and for this reason, the azimuthal antipodes evolve non-homogeneously, so they collide and form the structure shown in the plot. The faster these collisions occur due to the lack of symmetry, the faster the simulation finishes. This explain the range in ending times for the ResR models.

In the case of the turbulent models, all models show agreement with the evolution of the base simulation. Indeed, Fig 4.6 demonstrates the consistency of the time evolution between the base simulation and the model ResT[a]. The same consistency is presented with the ResT[s] model. This result is expected, since the number of initial particles affected by particle splitting is very small with respect to the number of particles in the ResR[s] models.
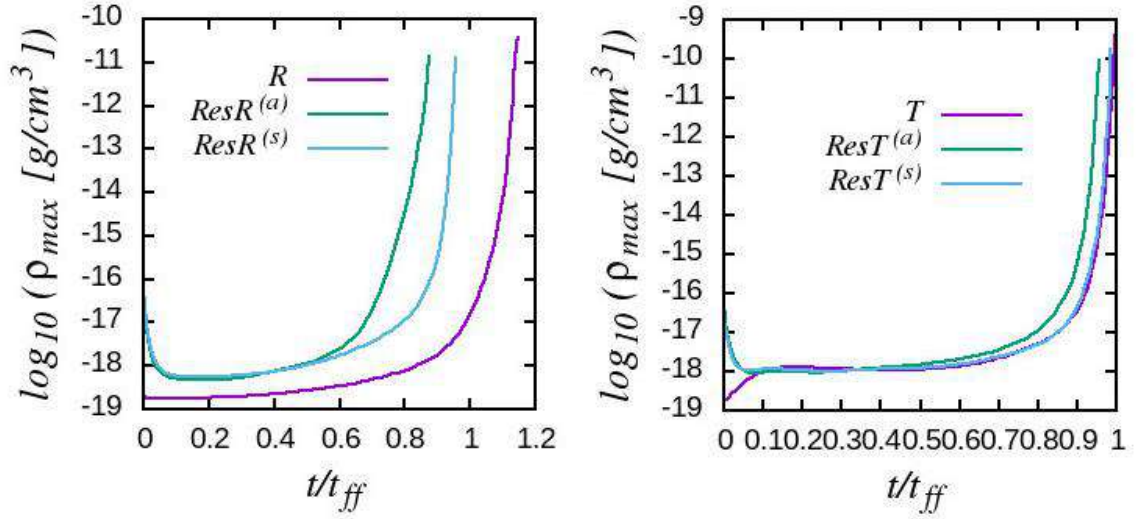
Fig. 4. 7. Time evolution of the peak density for the rotating models (left) and the turbulent models (right).

## 4.4 Characterization of the turbulent models

Larson (1981) proposed the empirical scaling relations

$$\rho \propto R^{\alpha} \tag{4.1}$$

$$\sigma_v \propto R^{\beta} \tag{4.2}$$

based on observational studies of molecular clouds and condensations. The most accepted values for the exponents are $\alpha \sim -1$ and $\beta \sim 0.5$ (Ballesteros-Paredes et al. 2018 and references therein). The first Larson relation (4.1)

$$\Sigma = \rho R \tag{4.3}$$

implies that the mean surface density of the cloud is roughly constant. From the second relation, eq. (4.2), the Larson's ratio can be defined as

$$\mathcal{L} = \frac{\sigma_v}{R^{1/2}} \tag{4.4}$$

The Larson's ratio has been traditionally interpreted as evidence of compressible turbulence (Ballesteros-Paredes et al. 2007 and references therein). For this reason, one can characterize

45

the turbulent models by plotting the Larson's ratio $\mathcal{L}$ versus the surface density $\Sigma$ for the different models. These are shown in fig 4.8. It is worth mentioning that as it has been possible to obtain measurements of such properties in regions of high surface density, the values of the exponents in the Larson's relations are not clear to be single valued, but a scatter plot (Ballesteros-Paredes et al. 2011a, 2018).

The procedure followed to generate the $\mathcal{L}$ *versus* $\Sigma$ plots is as follows:

First, the center of mass of the system is determined and using it as the coordinate origin, a radial partition of the system in terms of spherical shells, each of radius $R_i$, is made, where $i = 1, \dots, nbin$, with radial thickness $\delta R$. $nbin$ is fixed to 500 shells for all the models. Next, the number of particles contained in each radial shell is counted and divided by the surface area of the shell at that radius, which is $4\pi R_i^2$, to obtain the mass per area, which is an estimate of the surface density of the system, denoted by $\Sigma$. Using this, the average magnitude of the velocity of all the particles contained in that shell, $v_{ave}$, is determined. Then, calculate the velocity dispersion at each radial shell using the standard definition, which is $\sigma_v^2 = \sum_{i=0}^{n}(v_i - v_{ave})^2/(n-1)$. Thus, taking the definition of Larson ratio as in eq. (4.4) the value of $\mathcal{L}$ at each shell is determined. However, to compare this with the results reported by Ballesteros et al. (2018), plots of the Larson ratio versus the surface density are made for a fixed time. Fig 4.8 shows the plots for $t = t_{final}$. For the base model T there is a single curve where $\mathcal{L}$ goes from cero increasing approximately as $\Sigma^{1/2}$. For the modified models, curves have two pieces or two branches, $\Sigma \leq \Sigma_0$ and it is increasing; while for the second branch, $\Sigma \geq \Sigma_0$ and it is decreasing. In the first branch, $\mathcal{L}$ increases with $\Sigma$ until it reaches $\mathcal{L}_{peak}$ on $\Sigma_0$. On this peak, turbulence dissipates and $\mathcal{L}$ decreases developing the second branch until it vanishes with $\Sigma$.

### 4.4.1 Evolutionary trend of the turbulent models

In the previous section the curves for $\mathcal{L}$ *versus* $\Sigma$ for the different models were generated for a fixed time, specifically, for the end of the time evolution. In order to follow the evolution of the turbulence on the various systems, a single $\mathcal{L}$ and a single $\Sigma$ for each model, for each evolution timestep has to be defined. This is achieved by calculating the arithmetic average

per snapshot, taking into account all the values obtained in the radial partition defined above. Fig. 4.8 in the right panel, shows the radial average obtained per snapshot, drawn with cross points, so that each point in the plot represents a time in the evolution of the simulation. Fitting curves are shown as lines and are generated with the proposed analytical formula

$$(f\mathcal{L}) = b\Sigma^a \tag{4.5}$$

where $a$ and $b$ are free parameters, which must be determined by applying the least-squares method to the original data. It must be noted that the fitting curves were obtained by using the data of the growing branch of each point sequence.

Ballesteros et al. (2018) showed a set of values of $\mathcal{L}$ versus $\Sigma$ obtained observationally for core samples of different sizes, fig. 4.9. For massive dense cores with label G, like the ones considered in this work, values for $\mathcal{L}$ ranges between 1 and 10 and those for $\Sigma$ are around 1000.

To compare these results with the values shown in fig. 4.9, table 4.1, columns three and four include the values for $\Sigma$ and $\mathcal{L}$ obtained by using the proposed analytical formula (4.5) to fit the values of the simulation curves. Our values of $\mathcal{L}$ are too high, while our $\Sigma$ are too low, compared with the observational ones.


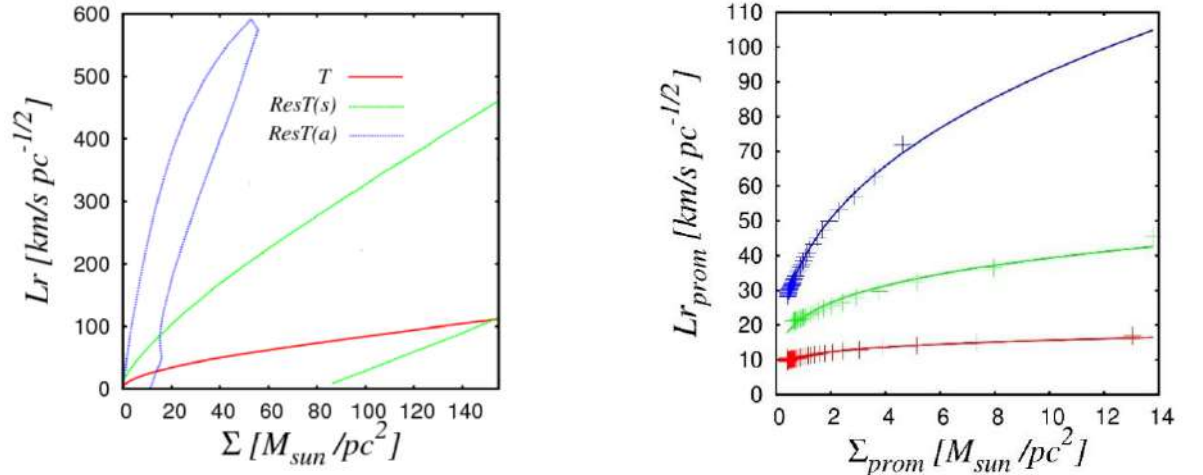
Fig. 4. 8. Larson ratio *versus* the surface density for the different turbulent models at $t = t_{final}$, left panel. Time evolution of the average-Larson ratio versus average-density surface for the different turbulent models, right panel.
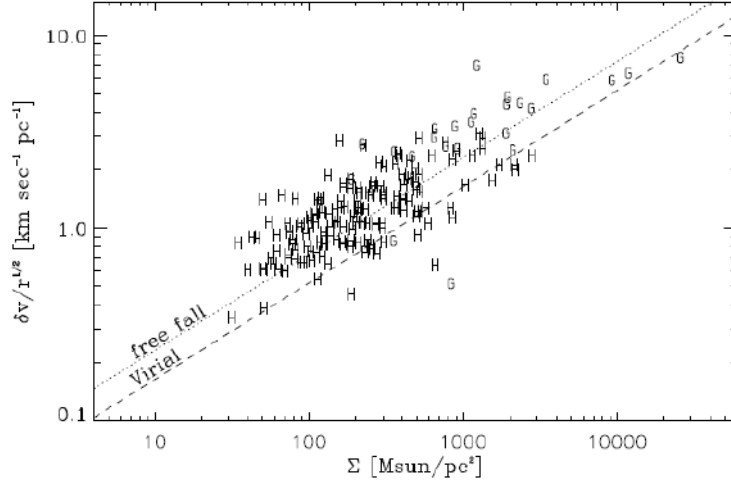
47

Fig. 4. 9. "Massive dense cores from Gibson et al. (2009, labeled "G"), and clouds and clumps from Meyer et al. (2009, labeled "H") in the $\sigma_v/R^{1/2}$ *versus* $\Sigma$ plane, where $\sigma_v$ is the velocity dispersion, $R$ is the region size, and $\Sigma$ is the mass column density. The straight lines show the loci of virial equilibrium, $|E_g| = 2E_k$, and of energy conservation under free-fall, $|E_g| = E_k$". Adapted from Vázquez-Semadeni (2010).

| Model | Label | $\Sigma_{ave}[M_{sun}/pc^2]$ | $L_{ave}[km/s\,pc^{-1/2}]$ |
|-------|-------|------------------------------|----------------------------|
| 4 | $T$ | 1.24 | 10.74 |
| 5 | $ResT\,^{a}_{z}$ | 0.87 | 36.03 |
| 6 | $ResT\,^{s}_{z}$ | 1.26 | 23.96 |

Table 4. 1. Dynamic parameters of turbulent models.
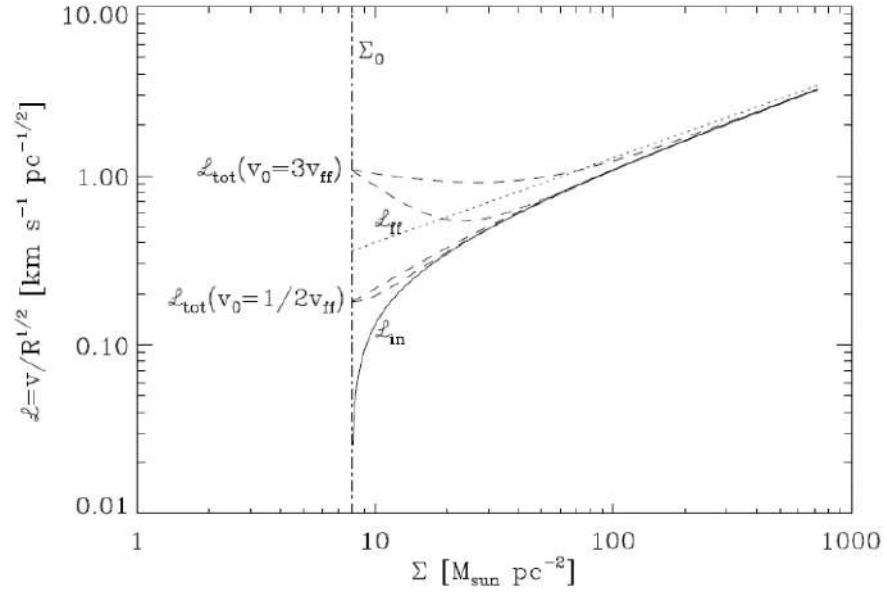
Fig. 4. 10. "The solid line shows the trajectory in the $\mathcal{L}$ vs $\Sigma$ plane of a core of fixed mass $M{=}1\ M_\odot$ that becomes Jeans-unstable, beginning to collapse at a time $t = 0$, at which it has an initial radius $R_0 = 0.2\ pc$. Implying an initial column density $\Sigma_0$, shown by the vertical dashed-dotted line". Adapted from Vázquez-Semadeni (2018).

# Chapter 4 – Discussion and Conclusions

In this work, a series of simulations of hydrodynamic self-gravitational collapse of dense gas cores were performed using the Gadget2 code for solving the SPH equations and the particle splitting technique for resolution enhancement in regions where high densities are reached. Simulations upon base models gave place to modified simulations were particle splitting was applied on two variants: First, applying particle splitting upon all the particles in the simulation, and the second variant, applying the technique upon a subset of the total number of particles.

The simulations of the base models, which are the core with rigid-body rotation and the turbulent core, have shown all the expected features and substructures at initial and final time evolution. In the case of the rotating models, at initial time, modified rotating models agree with base simulation although some unexpected effects over the density distribution due to the application of particle splitting can be seen on the modified models. It seems that particle splitting generates a mass perturbation different than that induced in the base simulation, ending with a quite different structure. The time evolution curves differ in that the modified simulations end earlier than the base one. All the models experience the same general behavior, in that all go into an initial expansion, then undergo a process of density lowering in which the peak density smooths quickly, since the particles go randomly in all spatial directions. Then, the real collapse begins. At this point new density perturbations have formed across the core. Then, the densest particles of the simulations form bar-like elongated structures, which may go through morphological transformations along the evolution.

In the case of the turbulent models, at initial time, modified turbulent models agree with each other and with the base simulation. Turbulent effects are not disturbed with the technique. The general behavior of the maximum peak density evolution is quite similar between them.

With respect to the characterization of turbulent models, the evolution of the Larson ratio with the surface density was seen to have similar behavior to the one shown in fig 4.10, however the results obtained give very small values for $\mathcal{L}$ and too large values for $\Sigma$. This can be seen in the dynamic parameters of table 4.1 for the various models.

The objectives of the work were fully achieved in the sense that simulations were performed with improved resolution for both the rotating and turbulent cores. Substructure and more features were possible to observe with the modified simulations but there is work left to do if one wants to improve the reliability on the rotating models in the search for a way to set fully properly the initial conditions with both particle splitting variants.

# Bibliography

Arreaga-García, G., 2017, Revista Mexicana de Astronomía y Astrofísica, 53, pp. 1–24.

Bagla, J. S. (2002). TreePM: A code for cosmological N-body simulations. *Journal of Astrophysics and Astronomy*, *23*(3-4), 185-196.

Ballesteros-Paredes, J., Hartmann, L., & Vázquez-Semadeni, E. (1999). Turbulent flow-driven molecular cloud formation: A solution to the post-T Tauri problem?. *The Astrophysical Journal*, *527*(1), 285.

Ballesteros-Paredes, J., Vázquez-Semadeni, E., Palau, A., & Klessen, R. S. (2018). Gravity or turbulence?–IV. Collapsing cores in out-of-virial disguise. *Monthly Notices of the Royal Astronomical Society*, *479*(2), 2112-2125.

Balsara, D. S. (1995). Von Neumann stability analysis of smoothed particle hydrodynamics Suggestions for optimal algorithms. *Journal of Computational Physics*, *121*(2), 357-372.

Barnes, J., & Hut, P. (1986). A hierarchical O (N log N) force-calculation algorithm. *nature*, *324*(6096), 446-449.

Bate, M. R., & Burkert, A. (1997). Resolution requirements for smoothed particle hydrodynamics calculations with self-gravity. *Monthly Notices of the Royal Astronomical Society*, *288*(4), 1060-1072.

Bate, M. R., Bonnell, I. A., & Price, N. M. (1995). Modelling accretion in protobinary systems. *Monthly Notices of the Royal Astronomical Society*, *277*(2), 362-376.

Bending, T.J. R., Dobbs, C.L. and Bate, M.R., 2020, MNRAS, 495, Issue 2, pp.1672-1691.

Bergin, E. and Tafalla, M., 2007, Annu. Rev. Astro. Astrophys., 45, 339.

Bodenheimer, P. (2011). *Principles of star formation*. Springer Science & Business Media.

Boss, A. P., & Bodenheimer, P. (1979). Fragmentation in a rotating protostar-A comparison of two three-dimensional computer codes. *The Astrophysical Journal*, *234*, 289-295.

Boss, A.P., Fisher, R.T., Klein, R. and McKee, C.F., 2000, ApJ, 528, 325.

Burkert, A., & Bodenheimer, P. (1993). Multiple fragmentation in collapsing protostars. *Monthly Notices of the Royal Astronomical Society*, *264*(4), 798-806.

Carr, D., Kahn, R., Sahr, K., & Olsen, T. (1997). ISEA discrete global grids. *Statistical Computing & Statistical Graphics Newsletter*, *8*(2/3), 31-39.

Dobbs, C.L., Bonnell, I.A. and Clark, P.C., 2005, MNRAS, 360, pp. 2-8.

Gingold, R. A., & Monaghan, J. J. (1977). Smoothed particle hydrodynamics: theory and application to non-spherical stars. *Monthly notices of the royal astronomical society*, *181*(3), 375-389.

Goldstein, H., Poole, C., & Safko, J. (2002). Classical mechanics.

Goodwin, S.P., Whitworth, A.P. and Ward-Thompson, D., 2004a, Astron. Astrophys., 414, pp. 633–650.

Goodwin, S.P., Whitworth, A.P., Ward-Thompson, D., 2004, Astron. Astrophys.,423, pp.169-182.

Goodwin, S.P., Whitworth, A.P., Ward-Thompson, D., 2006, Astron. Astrophys., 452, pp. 487-492.

Jijina, J., Myers, P.C. and Adams, C., 1999, ApJ, SUPPLEMENT SERIES, 125, pp.161-236.

Kenyon, S. J., Gomez, M., & Whitney, B. A. (2008). Low Mass Star Formation in the Taurus-Auriga Clouds. *arXiv preprint arXiv:0810.1298*.

Kitsionas, S. (2003). Particle Splitting: A New Method for SPH Star Formation Simulations. *arXiv preprint astro-ph/0307478*.

Kitsionas, S., & Whitworth, A. P. (2002). Smoothed particle hydrodynamics with particle splitting, applied to self-gravitating collapse. *Monthly Notices of the Royal Astronomical Society*, *330*(1), 129-136.

Klessen, R. S. (2001). The formation of stellar clusters: mass spectra from turbulent molecular cloud fragmentation. *The Astrophysical Journal*, *556*(2), 837.

Klessen, R. S., Heitsch, F., & Mac Low, M. M. (2000). Gravitational collapse in turbulent molecular clouds. I. Gasdynamical turbulence. *The Astrophysical Journal*, *535*(2), 887.

Landau, L. D., & Lifshitz, E. M. (1966). Mécanique quantique: théorie non relativiste.

Lucy, L. B. (1977). A numerical approach to the testing of the fission hypothesis. *The astronomical journal*, *82*, 1013-1024.

Meglicki, Z., Wickramasinghe, D., & Bicknell, G. V. (1993). 3D structure of truncated accretion discs in close binaries. *Monthly Notices of the Royal Astronomical Society*, *264*(3), 691-704.

Monaghan, J. J. (1988). An introduction to SPH. *Comput. Phys. Comm.*, *48*, 89-96.

Monaghan, J. J. (1992). Smoothed particle hydrodynamics. *Annual review of astronomy and astrophysics*, *30*(1), 543-574.

Monaghan, J. J. (1992). Smoothed particle hydrodynamics. *Annual review of astronomy and astrophysics*, *30*(1), 543-574.

Monaghan, J. J., & Gingold, R. A. (1983). Shock simulation by the particle method SPH. *Journal of computational physics*, *52*(2), 374-389.

Monaghan, J. J., & Lattanzio, J. C. (1985). A refined particle method for astrophysical problems. *Astronomy and astrophysics*, *149*, 135-143. pp.161-236.

Raskin, C., & Owen, J. M. (2016). Rapid Optimal SPH Particle Distributions in Spherical Geometries For Creating Astrophysical Initial Conditions. *The Astrophysical Journal*, *820*(2), 102.

Rey-Raposo, R., Dobbs, C. and Duarte-Cabral, A., 2015, MNRAS, 446, L46-L50.

Shu, C., & Richards, B. E. (1992). Application of generalized differential quadrature to solve two-dimensional incompressible Navier-Stokes equations. *International Journal for Numerical Methods in Fluids*, *15*(7), 791-798.

Springel, V. (2005). The cosmological simulation code GADGET-2. *Monthly notices of the royal astronomical society*, *364*(4), 1105-1134.

Springel, V., & Hernquist, L. (2002). Cosmological smoothed particle hydrodynamics simulations: the entropy equation. *Monthly Notices of the Royal Astronomical Society*, *333*(3), 649-664.

Tafalla, M., Myers, P.C., Caselli, P. and Walmsley, C.M.. 2004, °a, 416, 191.

Truelove, J. K., Klein, R. I., McKee, C. F., Holliman II, J. H., Howell, L. H., Greenough, J. A., & Woods, D. T. (1998). Self-gravitational hydrodynamics with three-dimensional adaptive mesh refinement: methodology and applications to molecular cloud collapse and fragmentation. *The Astrophysical Journal*, *495*(2), 821.

Vázquez-Semadeni, E., 2010, *Molecular Cloud Evolution*, published in "The Dynamic Interstellar Medium: A Celebration of the Canadian Galactic Plane Survey", ASP Conference Series, Vol. 438, R. Kothes, T. L. Landecker, and A. G. Willis eds.

Vázquez-Semadeni, E., Gómez, G. C., Jappsen, A. K., Ballesteros-Paredes, J., González, R. F., & Klessen, R. S. (2007). Molecular cloud evolution. II. From cloud formation to the early stages of star formation in decaying conditions. *The Astrophysical Journal*, *657*(2), 870.

Vázquez-Semadeni, E., Ryu, D., Passot, T., González, R. F., & Gazol, A. (2006). Molecular cloud evolution. I. Molecular cloud and thin cold neutral medium sheet formation. *The Astrophysical Journal*, *643*(1), 245.

Whitehouse, S.C. and Bate, M.R., 2006, MNRAS, 367,pp.32-38.


Xu, S., & Lazarian, A. (2020). Turbulence in a self-gravitating molecular cloud core. *The Astrophysical Journal*, *890*(2), 157.